JNeurosci
THE JOURNAL OF NEUROSCIENCE

Research Articles: Neurobiology of Disease

Systems Analysis of the 22q11.2 Microdeletion Syndrome Converges on a Mitochondrial Interactome Necessary for Synapse Function and Behavior

Avanti Gokhale[1], Cortnie Hartwig[1], Amanda A. H. Freeman[1,2], Julia L. Bassell[1], Stephanie A. Zlatic[1], Christie Sapp Savas[3], Trishna Vadlamudi[3], Farida Abudulai[3], Tyler T. Pham[13], Amanda Crocker[4], Erica Werner[5], Zhexing Wen[6], Gabriela M. Repetto[7], Joseph A. Gogos[8], Steven M. Claypool[9], Jennifer K. Forsyth[10], Carrie E. Bearden[10], Jill Glausier[11], David A. Lewis[11], Nicholas T. Seyfried[12], Jennifer Q. Kwong[13] and Victor Faundez[1]

[1]*Departments of Cell Biology, Emory University, Atlanta, GA, USA, 30322*
[2]*Center for the Study of Human Health, Emory University, Atlanta, GA, USA, 30322*
[3]*Department of Chemistry, Agnes Scott College, Decatur, Georgia 30030.*
[4]*Program in Neuroscience, Middlebury College, Middlebury, VT 05753.*
[5]*Radiation Oncology, Emory University, Atlanta, GA, USA, 30322*
[6]*Psychiatry, Emory University, Atlanta, GA, USA, 30322*
[7]*Centro de Genética y Genómica, Facultad de Medicina, Clínica Alemana Universidad del Desarrollo, Santiago, Chile.*
[8]*Departments of Neuroscience and Physiology, Columbia University, New York, NY 10032.*
[9]*Department of Physiology, The Johns Hopkins University School of Medicine, Baltimore, MD 21205.*
[10]*Semel Institute for Neuroscience and Human Behavior and Department of Psychology, UCLA, Los Angeles, CA, 90095.*
[11]*Departments of Psychiatry and Neuroscience, University of Pittsburgh, Pittsburgh, PA, 15213.*
[12]*Biochemistry, Emory University, Atlanta, GA, USA, 30322*
[13]*Pediatrics, Emory University, Atlanta, GA, USA, 30322*

https://doi.org/10.1523/JNEUROSCI.1983-18.2019

Received: 2 August 2018

Revised: 18 January 2019

Accepted: 15 February 2019

Published: 4 March 2019

Author contributions: A.G., C.H., A.F., S.A.Z., A.C., Z.W., C.E.B., D.A.L., J.Q.K., and V.F. designed research; A.G., C.H., A.F., J.L.B., S.A.Z., C.S.S., T.V., F.A., T.T.P., A.C., E.W., Z.W., G.M.R., J.K.F., C.E.B., J.G., D.A.L., N.T.S., and J.Q.K. performed research; A.G., C.H., A.F., J.L.B., S.A.Z., C.S.S., T.V., F.A., T.T.P., A.C., E.W., Z.W., G.M.R., J.K.F., C.E.B., J.G., D.A.L., J.Q.K., and V.F. analyzed data; A.G., C.H., A.F., J.L.B., S.A.Z., J.A.G., S.C., J.K.F., C.E.B., D.A.L., N.T.S., J.Q.K., and V.F. edited the paper; J.A.G., S.C., and N.T.S. contributed unpublished reagents/analytic tools; V.F. wrote the first draft of the paper; V.F. wrote the paper.

Conflict of Interest: The authors declare no competing financial interests.

This work was supported by grants from the National Institutes of Health R56 MH111459 to VF and Emory Catalyst Grant, Fondecyt-Chile grant 1171014 to GMR, R01HL108882 to SMC, R01MH097879 to JAG. CH is supported by the FIRST postdoctoral fellowship NIH 5K12GM000680. We thank members of the Faundez Lab for their comments and insight. Stocks obtained from the Bloomington ***Drosophila*** Stock Center (NIH P40OD018537) were used in this study. This study was supported in part by the Emory HPLC Bioanalytical Core (EHBC) and the Emory Imaging Core. EHBC is supported by the Department of Pharmacology, Emory

University School of Medicine and the Georgia Clinical & Translational Science Alliance of the National Institutes of Health under Award Number UL1TR002378.

Address Correspondence to VF (vfaunde@emory.edu) ORCID 0000-0002-2114-5271

Cite as: J. Neurosci 2019; 10.1523/JNEUROSCI.1983-18.2019

Systems Analysis of the 22q11.2 Microdeletion Syndrome Converges on a Mitochondrial Interactome Necessary for Synapse Function and Behavior.

Avanti Gokhale[1*], Cortnie Hartwig[1*], Amanda A. H. Freeman[1-2*], Julia L. Bassell[1*], Stephanie A. Zlatic[1], Christie Sapp Savas[3], Trishna Vadlamudi[3], Farida Abudulai[3], Tyler T. Pham[13], Amanda Crocker[4], Erica Werner[5], Zhexing Wen[6], Gabriela M. Repetto[7], Joseph A. Gogos[8], Steven M. Claypool[9], Jennifer K. Forsyth[10], Carrie E. Bearden[10], Jill Glausier[11], David A. Lewis[11], Nicholas T. Seyfried[12], Jennifer Q. Kwong[13], Victor Faundez[1#**].

Departments of Cell Biology[1], Center for the Study of Human Health[2], Radiation Oncology[5], Psychiatry[6], Biochemistry[12], Pediatrics[13], Emory University, Atlanta, GA, USA, 30322. Department of Chemistry, Agnes Scott College, Decatur, Georgia 30030[3]. Program in Neuroscience, Middlebury College, Middlebury, VT 05753[4]. Centro de Genética y Genómica, Facultad de Medicina, Clínica Alemana Universidad del Desarrollo, Santiago, Chile[7]. Departments of Neuroscience and Physiology, Columbia University, New York, NY 10032[8]. Department of Physiology, The Johns Hopkins University School of Medicine, Baltimore, MD 21205[9]. Semel Institute for Neuroscience and Human Behavior and Department of Psychology, UCLA, Los Angeles, CA, 90095[10]. Departments of Psychiatry and Neuroscience, University of Pittsburgh, Pittsburgh, PA, 15213[11].

.

[#]Address Correspondence to VF (vfaunde@emory.edu) ORCID 0000-0002-2114-5271

* These authors contributed equally ** Lead Contact

Abstract

Neurodevelopmental disorders offer insight into synaptic mechanisms. To unbiasedly uncover these mechanisms, we studied the 22q11.2 syndrome, a recurrent copy number variant, which is the highest schizophrenia genetic risk factor. We quantified the proteomes of 22q11.2 mutant human fibroblasts from both sexes and mouse brains carrying a 22q11.2-like defect, *Df(16)A+/-*. Molecular ontologies defined mitochondrial compartments and pathways as some of top ranked categories. In particular, we identified perturbations in the SLC25A1-SLC25A4 mitochondrial transporter interactome as associated with the 22q11.2 genetic defect. Expression of SLC25A1-SLC25A4 interactome components was affected in neuronal cells from schizophrenia patients. Furthermore, hemideficiency of the *Drosophila* SLC25A1 or SLC25A4 orthologues, dSLC25A1-sea and dSLC25A4-sesB, affected synapse morphology, neurotransmission, plasticity, and sleep patterns. Our findings indicate that synapses are sensitive to partial loss of function of mitochondrial solute transporters. We propose that mitoproteomes regulate synapse development and function in normal and pathological conditions in a cell specific manner.

Significance Statement

We address the central question of how to comprehensively define molecular mechanisms of the most prevalent and penetrant microdeletion associated with neurodevelopmental disorders, the 22q11.2 microdeletion syndrome. This complex mutation reduces gene dosage of ~63 genes in humans. We describe a disruption of the mitoproteome in 22q11.2 patients and brains of a 22q11.2 mouse model. In particular, we identify a network of inner mitochondrial membrane transporters as a hub required for synapse function. Our findings suggest that mitochondrial composition and function modulate the risk of neurodevelopmental disorders, such as schizophrenia.

Introduction

Single gene defects associated with neurodevelopmental disorders provide a fertile ground to uncover fundamental synaptic mechanisms. For example, mutations in FMR1, MECP2, DISC1, or NRXN1 associate with diverse mental and/or behavioral disorders, including autism spectrum disorder and schizophrenia. Understanding molecular mechanisms linking these single gene defects with pathways that impinge on synapse function has been significantly advanced (Ishizuka et al., 2006; Santoro et al., 2012; Bena et al., 2013; Wen et al., 2014; Sztainberg and Zoghbi, 2016). This fact is founded on well-established experimental paradigms that identify and test causality between a single gene defect, its downstream molecular mechanisms, and phenotypes. In contrast, there are a great number of neurodevelopmental disorders that associate with chromosomal microdeletions, in particular, hemizygous deletions containing multiple contiguous genes. Microdeletions have received great attention as they are the most penetrant and frequent genetic defects linked to neurodevelopmental disorders (Girirajan et al., 2011; Malhotra and Sebat, 2012; Sullivan et al., 2012; Kirov, 2015; Rutkowski et al., 2017). In comparison to monogenic disorders, the study of microdeletions is impeded by the lack of experimental paradigms that comprehensively capture contributions of all genes within the hemideletion to downstream molecular mechanisms and phenotypes (Iyer et al., 2018). Thus, the identity of molecular mechanisms downstream a whole microdeletion and their phenotypic impact in synapses remains elusive. Here we address this issue focusing on the 22q11.2 microdeletion syndrome.

The 22q11.2 microdeletion syndrome (OMIM #192430, #188400) (McDonald-McGinn et al., 2015) is the strongest and most prevalent genetic risk factor for schizophrenia increasing the overall risk of psychiatric pathology 20- to 25-fold as compared with the general population (Bassett et al., 2000; Hodgkinson et al., 2001; Bassett and Chow, 2008). Twenty five percent of 22q11.2 patients develop schizophrenia. In addition, the 22q11.2 microdeletion is the most common genetic defect found in sporadic cases of schizophrenia (Bassett et al., 2003; Bassett and Chow, 2008; International Schizophrenia, 2008; Karayiorgou et al., 2010; Jonas et al., 2014; Schneider et al., 2014; Hoeffding et al., 2017; Marshall et al., 2017). The strong association of mental and/or behavioral disorders with the 22q11.2 genetic defect makes this syndrome a robust model to test new experimental paradigms to identify molecular pathways and synaptic mechanisms downstream complex neurodevelopmental genetic defects.

We studied the most prevalent 22q11.2 microdeletion in humans, which encompasses three megabases. This microdeletion creates an haploinsufficiency of 46 protein coding genes and 17 regulatory small RNAs, thus opening the door for multiple pathways and organelles that could be affected downstream (Guna et al., 2015). We reasoned that top ranked molecular ontologies associated with the 22q11.2 genetic defect should enrich pathways and organelles implicated in mechanisms affecting synapse function and thus contribute to psychiatric phenotypes in humans. Using genealogical and integrated mass spectrometry-based

proteomics, we report the unbiased and statistically prioritized identification of pathways and organelles affected by the 22q11.2 microdeletion syndrome. Our comparative systems biology studies interrogated the proteome of fibroblasts from human pedigrees, genealogical proteomics, and the brain of a mouse model that genotypically and phenotypically mimics the 22q11.2 syndrome, the *Df(16)A+/-* deficiency (Karayiorgou et al., 2010). We conclude that the mitochondrion is a top ranked organelle affected in the 22q11.2 microdeletion syndrome. We propose that mitoproteomes modulate synapse development and function in normal and pathological states.

Material and Methods

Cell lines and Culture Conditions

Pedigrees of Ch22q11.2 fibroblasts were obtained from RUCDR Infinite Biologics repository (RUID: MH0162519, RUID: MH0162508, MH0162509, RUID: MH0162499, RUID: MH0162510, RUID: MH0162511, RUID: MH0162626, RUID: MH0162636, RUID: MH0162627, RUID: MH0162628, RUID: MH0162673, MH0162674, RUID: MH0162675, MH0162676, RUID: MH0162677, RUID: MH0162678). The fibroblasts were grown according to supplier recommendations in DMEM (Corning, 10-013- CV) media supplemented with 15% fetal bovine serum (FBS) (Atlanta Biologicals, S12450) and 100 µg/ml penicillin and streptomycin (Hyclone, SV30010) at 37°C in 5% CO_2. SH-SY5Y cells (ATCC, CRL-2266; RRID: CVCL_0019) were cultured in DMEM media supplemented with 10% fetal bovine serum and 100 µg/mL penicillin and streptomycin at 37°C in 10% CO_2. The SH-SY5Y cells were stably transfected either with a control empty vector (Genecopoeia, EX-NEG-Lv102) or ORF expression clone for N terminally tagged FLAG-SLC25A1 (Genecopoeia, EX-A1932-Lv1020GS) and grown in a selection media containing DMEM media supplemented with 10%FBS and Puromycin 2ug/ml (Invitrogen, A1113803). HEK293-Flp-In-pCDNA5/FRT-CNAP-Ant1/Ant2 (SLC25A4/SLC25A5) cells previously described (Lu et al., 2017). The cells were grown in DMEM media with 10%FBS and 100ug/ml Hygromycin (Invitrogen, 10687010). HAP1 cell lines – Control (C631), SLC25A1 knockout cell lines (HZGHC001753c003 and HZGHC001753c010) and SLC25A4 knockout cell line (HZGHC000778c011) were obtained from Horizon (RRID:CVCL_5G07, RRID:CVCL_TM04, RRID:CVCL_TM05, and RRID:CVCL_TM45). HAP1 cells were cultured in IMDM media (Lonza, 12-722F) supplemented with 10% FBS and 100ug/ml penicillin and streptomycin at 37°C in 10% CO_2.

Drosophila Husbandry and Stocks

Drosophila stocks were reared at 25°C in a humidified incubator (Shel Lab SR120PF) with a 12hr light/dark cycle and fed standard molasses food (900mL milli-Q water+48g active dry yeast+120g cornmeal+9g agar+120g molasses+2.4g tegosept+9mL propionic acid). The following stocks were used w[1118] (BDSC Cat# 3605, RRID:BDSC_3605), C155-GAL4 (P{w[+mW.hs]=GawB}elav[C155]) (RRID:BDSC_458), Ddc-GAL4 (w[1118];P{w[+mC]=Ddc-GAL4.L}Lmpt[4.36] RRID:BDSC_7009) were obtained from the Bloomington Drosophila Stock Center. Gal4 lines used: c739 (α/βKC), NP1131 (γKC), R27G01 (MBON-γ5β'2a), R71D08(V2), G0431 (DAL). R27G01 (RRID:BDSC_49233), G0239 (12639), G0431 (12837) and UAS-2xeGFP(RRID:BDSC_6874) were ordered from the Bloomington Stock Center. NP1131-Gal4 was ordered from DGRC Stock center. R71D08 was a kind gift from Dr. H. Tanimoto. 3-86-Gal4 was a kind gift from Dr. U. Heberlein. c739-Gal4 was a kind gift from Dr. A. Sehgal. All Gal4 lines were crossed with UAS-2xeGFP to allow for cell harvesting.

yw;;UAS-GFP-AP4mito[55] (BSC 25748) and ;;seaΔ^{24}/TM3,Sb,Dfd::YFP (gift from Giovanni Cenci and Jason Tennessen). c155-GAL4;; flies were crossed to yw;;UAS-GFP-AP4mito[55]. Progeny were then crossed to either: ;;seaΔ^{24}/TM3,Sb,Dfd::YFP or sesB^{org};; and larval progeny selected for GFP expression prior to dissection.

Human Subjects

Seventy-seven patients with a molecularly confirmed diagnosis of 22q11DS and 50 unaffected, demographically matched healthy controls who were part of an ongoing longitudinal study at the University of California, Los Angeles were included in the current analyses. 22q11DS participants were recruited from posts to 22q11DS/Velocardiofacial online foundations and flyers through contacts with local craniofacial or genetics clinics. Controls were recruited from flyers posted at local schools and community centers. The study was approved by the UCLA Institutional Review Board and performed in accordance with the Declaration of Helsinki. All subjects or their legal guardians provided written informed consent and/or assent. This cohort has been previously published (Jalbrzikowski et al., 2015)

All data from the studies performed in postmortem human brain tissue have been previously published (Arion et al., 2015; Enwright Iii et al., 2017), and all methods and materials descriptions and data are publicly available (Arion et al., 2015; Enwright Iii et al., 2017).

Antibodies

Antibodies used for immunoblots were as follows – SLC25A1 (Proteintech, 15235-1-AP; RRID: AB_2254794), SLC25A4 (1F3F11, a gift from the Claypool laboratory, Johns Hopkins), β-Actin (Sigma-Aldrich, A5441; RRID: AB_476744), HSP90 (BD Biosciences, 610418; RRID: AB_397798), TFRC (Invitrogen, 13-6800; RRID: AB_86623), FLAG (Bethyl, A190-102A; RRID: AB_67407). Blotting secondary antibodies were against mouse or rabbit conjugated to HRP (ThermoFisher Scientific, A10668; RRID: AB_2534058 and G21234; RRID: AB_2536530).

Cell Lysis and Immunoprecipitation

Cells intended for immunoprecipitation (Control HAP1 cells, HAP1 with SLC25A1/SLC25A4 knockdowns, SH-SY5Y empty vector or SH-SY5Y transfected with FLAG-SLC25A1 or HEK293-Flp-In-pCDNA5/FRT-CNAP-Ant1/Ant2 cells) were placed on ice, rinsed twice with ice cold PBS (Corning, 21-040-CV) containing 0.1mM CaCl2 and 1.0mM MgCl2. The cells were then rinsed twice with PBS and lysed in buffer A (150 mM NaCl, 10 mM HEPES, 1 mM EGTA, and 0.1 mM $MgCl_2$, pH 7.4) with 0.5% TritonX-100 and Complete anti-protease (Roche, 11245200). Cells were scraped from the dish, placed in Eppendorf tubes, followed by incubation for 30 minutes on ice. Cell homogenates were then centrifuged at 16,100×*g* for 10 minutes and the clarified supernatant was recovered. Protein concentration determined using the Bradford Assay (BioRad, 5000006). For immunoprecipitation, 500 µg of protein extract was incubated with 30 microliters Dynal magnetic beads (Invitrogen, 110.31) coated with antibody,

and incubated for 2 hours at 4°C. In some cases, immunoprecipitations were done in the presence of the antigenic 3X FLAG peptide (340µM) (Sigma, F4799) as a control. The beads were then washed 4-6 times with buffer A with 0.1% TritonX-100. Proteins were eluted from the beads with Laemmli buffer. Samples were resolved by SDS-PAGE and contents analyzed by immunoblot described below.

Quantitative Mass Spectrometry

Proteomic services were provided by MS Bioworks (http://www.msbioworks.com/) or the Emory Integrated Proteomics Core (https://www.cores.emory.edu/eipc/).

Stable Isotope Labeling of Amino Acids (SILAC)

Ch22q11.2 fibroblasts were labeled using published protocols. Cells were cultured in DMEM with either "light" unlabeled arginine and lysine amino acids (R0K0) (Dundee Cell Products, LM014) "medium" 13C- and 15N-labeled arginine, and 13C- and 15N-labeled lysine amino acids (R6K4) (Dundee Cell Products, LM016) or "heavy" 13C- and 15N-labeled arginine, and 13C- and 15N-labeled lysine amino acids (R10K8) (Dundee Cell Products, LM015) supplemented with 15% FBS (Dundee Cell Products, DS1003) and 100 µg/ml penicillin and streptomycin. Each cell line was grown for seven passages allowing maximum incorporation (at least 97.5%) of the amino acids in the total cellular pool. Cellular lysate samples were prepared, as described in the previous section. Quantitative mass spectrometry was performed as described previously using the services of MS Bioworks and the Emory Integrated Proteomics Core.

The SILAC labeled samples were pooled 1:1:1 and 20µg of this mix was resolved on a 4-12% Bis-Tris Novex mini-gel (Invitrogen) using the MOPS buffer system. The gel was stained with Coomassie and the lanes excised into 40 equal sections using a grid. Gel pieces were robotically processed (ProGest, DigiLab) by first washing with 25mM ammonium bicarbonate (ABC) followed by acetonitrile, followed by reduction with 10mM dithiothreitol at 60°C, alkylation with 50mM iodoacetamide at room temperature. Pieces were digested with trypsin (Promega) at 37°C for 4h and quenched with formic acid. The supernatant was analyzed directly without further processing. Gel digests were analyzed by nano LC/MS/MS with a Waters NanoAcquity HPLC system interfaced to a ThermoFisher Q Exactive. Peptides were loaded on a trapping column and eluted over a 75µm analytical column at 350nL/min; both columns were packed with Jupiter Proteo resin (Phenomenex). The mass spectrometer was operated in data-dependent mode, with MS and MS/MS performed in the Orbitrap at 70,000 FWHM resolution and 17,500 FWHM resolution, respectively. The fifteen most abundant ions were selected for MS/MS. Data were processed through the MaxQuant software 1.4.1.2 which served the following functions: 1. Recalibration of MS data. 2. Filtering of database search results at the 1% protein and peptide false discovery rate (FDR). 3. Calculation of SILAC heavy:light ratios. Data

were searched using a local copy of Andromeda with the following parameters: Enzyme: Trypsin. Database: Swissprot (concatenated forward and reverse plus common contaminants). Fixed modification: Carbamidomethyl (C). Variable modifications: Oxidation (M), Acetyl (Protein N-term), $^{13}C_6/^{15}N_2$ (K), $^{13}C6/^{15}N_4$ (R), $^{4}H_2$ (K), $^{13}C_6$ (R). Fragment Mass Tolerance: 20ppm. Pertinent MaxQuant settings were: Peptide FDR 0.01. Protein FDR 0.01. Min. peptide Length 7. Min. unique peptides 0. Min. ratio count 2. Re-quantify TRUE. Second Peptide TRUE.

Label-free Quantitation (LFQ) cellular preparation

Cells were grown in 10cm dishes to 85-90% confluency. On the day of the experiment the cells were placed on ice and washed 3 times with PBS supplemented with 10mM EDTA (Sigma, 150-38-9) for 3 minutes each. After the third wash, the cells were incubated with PBS and 10mM EDTA for 30 minutes on ice. Cells were then lifted with mechanical agitation using a 10ml pipette and collected in a 15ml falcon tube. Cells were then spun at 800xg for 5 minutes at 4°C. The supernatant was then aspirated out and the remaining pellet was washed with ice cold PBS. The resuspended cells were then centrifuged at 16,100×*g* for 5 min. The supernatant was discarded and the resulting pellet was immediately frozen on dry ice for at least 5 minutes and stored at -80°C for future use.

Cell pellets were lysed in 200ul of urea lysis buffer (8M urea, 100 mM NaH2PO4, pH 8.5), supplemented with 2 uL (100x stock) HALT protease and phosphatase inhibitor cocktail (Pierce). Lysates were then subjected to 3 rounds of probe sonication. Each round consisted of 5 seconds of activation at 30% amplitude and 15 of seconds of rest on ice. Protein concentration was determined by bicinchoninic acid (BCA) analysis and 100 ug of each lysate was aliquoted and volumes were equilibrated with additional lysis buffer. Aliquots were diluted with 50mM ABC and was treated with 1mM DTT and 5mM IAA in sequential steps. Both steps were performed in room temperature with end to end rotation for 30 minutes. The alkylation step with IAA was performed in the dark. Lysyl endopeptidase (Wako) was added at a 1:50 (w/w) enzyme to protein ratio and the samples were digested for overnight. The following morning, a 50ug aliquot was taken out, acidified to a final concentration of 1% formic acid and stored. Trypsin (Promega) was added to the residual 50ug aliquot at a 1:100 (w/w) and digestion was allowed to proceed overnight again. Resulting peptides from both digestions rounds were desalted with a Sep-Pak C18 column (Waters).

Dried peptide fractions were resuspended in 100 µl of peptide loading buffer (0.1% formic acid, 0.03% trifluoroacetic acid, 1% acetonitrile). Peptide mixtures were separated on a self-packed C18 (1.9 µm Dr. Maisch, Germany) fused silica column (25 cm × 75 µm internal diameter; New Objective) by mass spectrometer platforms: 1) Dionex Ultimate 3000 RSLCNano coupled to a Fusion orbitrap tribrid mass spectrometer (ThermoFisher Scientific) and 2) Water's NanoAcquity coupled to a Q-Exactive Plus hybrid mass spectrometer (ThermoFisher Scientific) . For the Fusion system, 2ul was loaded and elution was carried out over a 140 min gradient at a rate of 300 nl/min with buffer B ranging from 3% to 99% (buffer A: 0.1% formic acid in water,

buffer B: 0.1% formic in acetonitrile). The mass spectrometer cycle was programmed to collect at the top speed for 5 s cycles consisting of 1 MS scan (400-1600 m/z range, 200,000 AGC, 50 ms maximum ion time) were collected at a resolution of 120,000 at m/z 200 in profile mode followed by ion trap collected HCD MS/MS spectra (0.7 m/z isolation width, 30% collision energy, 10,000 AGC target, 35 ms maximum ion time). Dynamic exclusion was set to exclude previous sequenced precursor ions for 20 s within a 10 ppm window. Precursor ions with +1 and +8 or higher charge states were excluded from sequencing. For the Q-Exactive Plus system, 4 ul was loaded and elution was carried out over a 140 min gradient at a rate of 250nl/min with buffer B ranging from 3 to 80% ACN. The mass spectrometer was set to acquire 1 MS scan (70,000 resolution at 200 m/z in profile mode, 300-1800 m/z range, 1,000,000 AGC, 100 ms maximum ion time) followed by at most 10 MS/MS scans(17,500 resolution at 200 m/z, 2.0 m/z isolation width with an offset of 0.5 m/z, 50,000 AGC, 50 ms maximum ion time). Dynamic exclusion was for 30 s with a 10 ppm window.

All spectra from both platforms were loaded into Maxquant (version 1.5.2.8) and searched against a database downloaded from the NCBI's REFSEQ (version 54) with common contaminants appended. Search parameter included fully tryptic (or lysyl endopeptidase) cleavage, variable modifications for Protein N-terminal acetylation and methionine oxidation, static modifications for cysteine carbamindomethyl, 20 ppm precursor mass tolerance, 0.5 Da for ion trap and .05 Da for Orbitrap product ion tolerances, FDR at 1% for all levels including protein, peptide and psm.

Tandem Mass Tagging (TMT)

Cell pellets were lysed, reduced, alkylated and digested similarly as with the LFQ protocol with the only differences being that 50mM TEAB was used for dilution and only Lysyl endopeptidase was used for digestion. An aliquot equivalent to 10 ug of total protein was taken out of each sample and combined to obtain a global internal standard (GIS) use later for TMT labeling.

TMT labeling was performed according to the manufacturer's protocol. Briefly (Ping et al., 2018), the reagents were allowed to equilibrate to room temperature. Dried peptide samples (90 µg each) were resuspended in 100 µl of 100 mm TEAB buffer (supplied with the kit). Anhydrous acetonitrile (41 µl) was added to each labeling reagent tube and the peptide solutions were transferred into their respective channel tubes. The reaction was incubated for 1 h and quenched for 15 min afterward with 8 µl of 5% hydroxylamine. All samples were combined and dried down. Peptides were resuspended in 100 µl of 90% acetonitrile and 0.01% acetic acid. The entire sample was loaded onto an offline electrostatic repulsion–hydrophilic interaction chromatography fractionation HPLC system and 40 fractions were collected over a time of 40 min. The fractions were combined into 10 and dried down. Dried peptide fractions were resuspended in 100 µl of peptide loading buffer (0.1% formic acid, 0.03% trifluoroacetic acid, 1% acetonitrile). Peptide mixtures (2 µl) were separated on a self-packed C18 (1.9 µm Dr.

Maisch, Germany) fused silica column (25 cm × 75 µm internal diameter; New Objective) by a Dionex Ultimate 3000 RSLCNano and monitored on a Fusion mass spectrometer (ThermoFisher Scientific). Elution was performed over a 140 min gradient at a rate of 300 nl/min with buffer B ranging from 3% to 80% (buffer A: 0.1% formic acid in water, buffer B: 0.1% formic in acetonitrile). The mass spectrometer cycle was programmed to collect at the top speed for 3 s cycles in synchronous precursor selection mode (SPS-MS3). The MS scans (380-1500 m/z range, 200,000 AGC, 50 ms maximum ion time) were collected at a resolution of 120,000 at m/z 200 in profile mode. CID MS/MS spectra (1.5 m/z isolation width, 35% collision energy, 10,000 AGC target, 50 ms maximum ion time) were detected in the ion trap. HCD MS/MS/MS spectra (2 m/z isolation width, 65% collision energy, 100,000 AGC target, 120 ms maximum ion time) of the top 10 MS/MS product ions were collected in the Orbitrap at a resolution of 60000. Dynamic exclusion was set to exclude previous sequenced precursor ions for 30 s within a 10 ppm window. Precursor ions with +1 and +8 or higher charge states were excluded from sequencing.

MS/MS spectra were searched against human database from REFSEQ (version 54) and Uniprot (downloaded on 03/06/2015) with Proteome Discoverer 1.4 and 2.0 (ThermoFisher Scientific), respectively. Methionine oxidation (+15.9949 Da), asparagine, and glutamine deamidation (+0.9840 Da) and protein N-terminal acetylation (+42.0106 Da) were variable modifications (up to 3 allowed per peptide); static modifications included cysteine carbamidomethyl (+57.0215 Da), peptide n terminus TMT (+229.16293 Da), and lysine TMT (+229.16293 Da). Only fully cleaved Lysyl endopeptidase peptides were considered with up to two miscleavages in the database search. A precursor mass tolerance of ±20 ppm and a fragment mass tolerance of 0.6 Da were applied. Spectra matches were filtered by Percolator to a peptide-spectrum matches false discovery rate of <1%. Only razor and unique peptides were used for abundance calculations. Ratio of sample over the GIS of normalized channel abundances were used for comparison across all samples.

Electrophoresis and Immunoblotting

For western blot, lysate was reduced and denatured in Laemmli buffer containing SDS and 2-mercaptoethanol and heated for 5 minutes at 75°C. Equal amounts of cellular lysates were loaded onto 4-20% Criterion gels (BioRad, 5671094) for electrophoresis and transferred to PVDF (Millipore, IPFL00010) using the semi-dry transfer method. The PVDF membranes were blocked with Tris buffered saline containing 5% non-fat milk and 0.05% Triton X-100 (TBST), rinsed and incubated overnight in presence of appropriately diluted primary antibody in antibody base solution (PBS with 3% Bovine Serum Albumin, 0.2% Sodium Azide). Membranes were then washed multiple times in TBST and incubated in HRP conjugated secondary antibody diluted 1:5000 in the blocking solution above. Following multiple washes, the membranes were then exposed to Amersham Hyperfilm ECL (GE Healthcare, 28906839) with Western Lightning Plus ECL reagent (Perkin Elmer, NEL105001EA).

Cell Line RNA Extraction and Quantitative RT-PCR

RNA extraction for cells and tissues was done using Trizol Reagent (Invitrogen, 15596026) following the published protocol. Total amount, concentration and purity of RNA were determined using the BioRad SmartSpec Plus Spectrophotometer. First strand synthesis was completed using the Superscript III First Strand Synthesis System Kit (Invitrogen, 18080-051) utilizing 5 μg total RNA per reaction and random hexamer primers following manufactures protocol. RT-PCR was done with 1μl cDNA from first strand synthesis in LightCycler 480 SYBR Green I Master (Roche, 04707516001) according to manufactures protocol on a LightCycler 480 Instrument with 96-well format. RT-PCR protocol included an initial denaturation at 95° C for 5min, followed by 45 cycles of amplification with a 5 second hold at 95°C ramped at 4.4°C/s to 55°C. Temperature was then held for 10 seconds at 55°C and ramped up to 72°C at 2.2°C/s. Temperature was held at 72°C for 20 seconds were a single acquisition point was collected and then ramped at 4.4°C/s to begin the cycle anew. A melting curve was collected following amplification. The temperature was then held at 65° for 1 min and ramped to 97°C at a rate of 0.11°C/s. Five acquisition points were collected per °C. Primers were designed using the IDT Real Time qPCR Assay Entry site using site recommended parameters. Primers were obtained from Sigma Custom DNA Oligo service. Melting curves were used to confirm primer specificity to single transcripts. Primer list is provided in Table 1. For quantification, standard curves for each primer were applied to all samples using LightCycler 480 software. Ratios of experimental to control samples, normalized to reference genes, are reported.

Drosophila Neuromuscular Microcopy

Neuromuscular junction staining was performed using late third instar larvae. Larval body wall dissections using a dorsal incision were performed with 10mM cell culture dishes partially filled with charcoal infused sylguard, microdissection pins, forceps and microdissection scissors. Drosophila were dissected using in standard Ca2+ free HL3 Ringer's Solution (70mM NaCl, 5mM KCl, 21.5mM MgCl2, 10mM NaHCO3, 5mM Trehalose, 115mM Sucrose, 5mM BES with pH of 7.2-7.3), fixed using 4% paraformaldehyde for 45minutes-1hour at room temp, rinsed 10minutes with PBS-T (PBS+.15% Triton), incubated in FITC-HRP conjugate (MP Biomedicals #0855977) overnight at 4C. Rinses followed the next day in PBS-T at 3x1minute rinse then 3x10minute rinse and finished with a 3x1minute rinse in PBS. Larval body wall preparations were then placed on slides with a drop of Vectashield and coverslip. Nail polish was used to seal the edges of the coverslip in place and samples were stored at 4C until imaged. Confocal images were obtained using a Zeiss LSM 510 microscope and Zen 2009 software. NMJs from 6/7 muscles of the 3rd or 4th segments were identified and z-stack images collected with a continuous wave 458,488nm argon laser at 200mW. Z-stacks were converted to jpegs using FIJI software and blinded for bouton quantification.

For mitochondrial stainings, third instar larvae were dissected in normal HL3 (Ca^{2+} free) and fixed in 4% paraformaldehyde at 25°C for 45 min-1 hr. Samples were briefly rinsed with PBS-T (PBS + .15% Triton-X) for 10 min. Primary antibody was then applied to the samples overnight at 4°C. Primary antibody consisted of rabbit anti GFP at 1:1000 (Sysy 132002 RRID:AB_887725), Cy3-HRP at 1:1000 (Santa Cruz 166894 HRP (RRID:AB_10614143)) and Alexa 633-phalloidin at 1:500 (Invitrogen A22284) in PBS-T. Samples were then rinsed in PBS-T. Secondary antibody was applied for 2 h at 25°C. Secondary antibody consisted of Alexa 488-goat anti rabbit at 1:1000 (Molecular Probes 10453272) plus additional Cy3-HRP at 1:1000 and Alexa 633-phalloidin at 1:500 in PBS-T. NMJs were imaged on an Olympus FV1000 Confocal Microscope at 20X. Oib files were converted to jpegs using Fiji software (RRID:SCR_002285). 8-bit jpegs were cropped to selected ROIs. Threshold was then adjusted to accurately highlight the fluorescent signal of both of the mitochondrial (GFP) and neuronal (Cy3) images for each NMJ. The Create Selection command was then used to outline the fluorescence in each image and measured using the ROI Manager tool. GFP/Cy3 signal ratios were then calculated for each genotype.

Drosophila Electrophysiology

NMJ dissections of third instar, female larvae were performed in ice-cold, calcium-free HL-3 Ringer's solution (70mM NaCl, 5mM KCl, 21.5mM $MgCl_2$, 10mM $NHCO_3$, 5mM Trehalose, 115mM Sucrose, 5 mM BES in ddH_20 with a pH of 7.2-7.3). After the dissection, the filleted preparation was rinsed twice in low-Ca^{2+} Ringer's solution (70mM NaCl, 5mM KCl, 1mM $CaCl_2$, 20mM $MgCl_2$, 10mM $NHCO_3$, 5mM Trehalose, 115mM Sucrose, 5 mM BES in ddH_20 with a pH of 7.2-7.3) and the low-Ca^{2+} Ringer's solution was used throughout the remainder of the experiment. Motor axons were severed close to the ventral ganglion and were taken up into a borosilicate glass capillary suction electrode with a firepolished tip (Microforge MF-830, Narishige). Recording electrodes were prepared using borosilicate glass capillary tubes (1mm outer diameter and 0.58 internal diameter; A-M Systems) which were pulled to a fine tip (PN-3, Narishige) with 25-50 MOhm resistance and backfilled with 3M KCl. All recordings were obtained from muscle 6 in the second or third abdominal sections (A2 or A3, respectively). Stimulations were delivered using a Model 2100 Isoplated Pulse Stimulator (A-M Systems) and recordings were acquired with an Axoclamp 900A amplifier (Molecular Devices). pClamp 10 software (Molecular Devices; RRID:SCR_011323) was used to collect data and analyzed EJP amplitude and membrane potential and Mini Analysis Program (Synaptasoft; RRID:SCR_002184) was used to analyze mEJPS frequency and amplitude.

Paired pulse facilitation (PPF) and mEJP data were collected from muscle 6 of segments 3 or 4 in late 3rd instar female larvae of the indicated genotypes (see Figure 8). Recordings had a resting membrane potential between -55 and -90mV and a muscle input resistance of >10MΩ. Recordings were performed in normal HL3 with pH of 7.2 with either low Ca^{2+} (in

mM): 70 NaCl, 5 KCl, 2.1 $MgCl_2$, 11.5 sucrose, .5 CaCl, 10 $NaHCO_3$, 5 trehalose and 5 BES or high Ca^{2+} (in mM): 70 NaCl, 5KCl, 1.95 $MgCl_2$, 11.5 sucrose, 2 CaCl, 10 $NaHCO_3$, 5 trehalose and 5 BES. For all PPF recordings, signals were acquired with Axoclamp 900A, digitized with Digidata 1440A and recorded with Clampfit 10.1. mEJPs were recorded by stimulating at 1Hz for 50s. mEJP analysis was performed with Mini Analysis (Synaptosoft RRID:SCR_002184) and Microsoft Excel (RRID:SCR_016137). PPF recordings were recorded by stimulating paired EJPs at 10Hz with a 2ms pulse duration and a 25ms interval between stimuli. PPF analysis was done with Axograph 1.7.2 (RRID:SCR_014284), Clampfit 10.7 (RRID:SCR_011323), and Microsoft Excel.

Drosophila Behavior (Sleep)

Female flies were collected under CO_2 anesthesia within 72 hours of eclosure. Twenty-four hours later, flies were briefly cooled on ice to allow mouth pipetting of individual flies into polycarbonate tubes (5mm external diameter x 65mm; TriKinetics.com). One end of the tube contained a 5% (w/v) sucrose and 2% (w/v) agarose medium while the other end was sealed with parafilm perforated with an 18-gauge needle to allow air circulation. Tubes were placed in the *Drosophila* Acitivity Monitoring System (DAM2; TriKinetics) which was housed in a light-controlled cabinet with a 12h:12h light:dark cycle at room temperature.

Data was collected in 15 second intervals using the DAMSystem308 acquisition software (TriKinetics) and analysis was based upon 1-minute bins across 6 days of data collection, starting at Lights ON the day after the animals were placed in the tubes. Periods of inactivity lasting longer than 5 minutes were scored as sleep (Hendricks et al. 2000, Shaw et al. 2000) and sleep duration, bout number, and bout length were calculated using a custom created analysis in Excel. All genotypes were compared to Canton S. Each UAS- and Gal4- line was crossed to Canton S to verify that neither the presence of the transgenes nor the genetic background of these individual lines altered the sleep/wake phenotype. Sleep/wake phenotypes of the sesB mutants were assessed based upon homozygous populations of the hypomorphic $sesB^{org}$ mutation and heterozygous populations of the lethal $sesB^{9Ed-1}$ mutation ($sesB^{9Ed-1}$/FM7a;;).

Drosophila RNAseq library generation

Cell harvesting

GFP labeled cells were handpicked in vivo through suction into a pipette. Cells designated for sequencing were harvested into .5ul nuclease free water in the pipette tip and then the tip was broken into a 96 well PCR tube containing RNAse inhibitors and buffer as described by Clontech's ultra low HV SMARTer Ultra Low RNAseq kit (Catalog# 634823) resulting in the lysing of cells without mechanical means. Amplification was performed following the Clontech Ultra-Low volume SMARter RNAseq Protocol. For the DAL neuron, the MBONα3 neurons, the MBON-γ5β'2a and MBON-β2β'2a neurons, 4 cells were pooled into each

tube thus these samples contained cells from more than one fly. For the V2, α/βKCs and γKCs all cells were taken from one animal per sample. V2 samples contained 14 cells and the α/βKC and γKC samples contained about 100 cells. 15 rounds of PCR amplification were performed using the Clontech SMARTer Ultra low RNAseq Kit. For this work only cells collected from animals that had undergone unpaired odor and shock presentation were used.

Following amplification samples were selected if there was a peak around 7 kb and .4-2ng/ul of product between the range 400bp-10kb. Samples were then sheared using a Covaris LE220 sonicator to 200bp. The libraries were made using the IntegenX automated library prep system. The PrepX Illumina DNA library prep kit/ PrepX CHIPseq kit (WaferGen Biosystems Inc) was used with an amplification of 17-22 cycles. They were multiplexed using Bioo Scientific barcodes. Then cleaned using the IntegenX PCR cleanup kit. Libraries were run on the Illumina HiSeq2500, 12 samples per lane and each sample run across two lanes. Resulting in a sequencing depth of 30 million reads. Sequencing was all done single end.

Analysis of Sequencing Reads

FastQC (Andrews, 2012) was performed to remove samples of poor quality. Samples all contained a bias for polyA and T sequences. This was uniform across all samples and was removed from sequences prior to mapping. GC content was not flagged on samples used in the study. All mapping was performed using Princeton University's Galaxy server running TopHat 2 with Bowtie2 (Kim et al.2013, (Langmead and Salzberg, 2012). The Ensembl build of the reference sequence (BDGF 5.25) and the GTF files were used and can acquired from iGenome (illumina). The aligned SAM/BAM file were processed using HTseq-count (Intersection mode - strict) (Anders et al., 2015). HTseq Counts output files and raw illumine read files are publicly available (GEO with accession number GSE4989). The HTseq counts compiled file is GSE74989_HTseqCountscompiledData.txt.gz

Calculating Normalized Gene Counts

The GSE74989_HTseqCountscompiledData.txt.gz data set was used for analysis. In R, all genes with counts less than 2 counts per million (8 counts) across all samples independent of cell-type were considered noise and removed from analysis. Gene counts were normalized using DESeq2 (Love et al., 2014) followed by a regularized log transformation. Genes with less than 2 counts per million within cell-type were recoded as zero. Principal component analysis was performed on this processed data set in R. R function prcomp was used to generate the principle components and gene loading values.

Drosophila Transcriptome Encoding Mitochondrial Proteins

All data was acquired from the GEO data set GSE74989 which is publicly available. From this data set only control animals were used to generate the figure and cell-type results. Thus 5 DAL samples, 5 V2 samples, 5 a/b KC samples, 5 gKC samples, 5 MBON b2b'2a, 4 MBON g5b'2a.

Human Postmortem RNA Analysis

All data from the studies performed in postmortem human brain tissue have been previously published. All tissue sample collection and RNA sequencing (RNASeq) details are publicly available (https://www.synapse.org/#!Synapse:syn2759792/wiki/). All tissue sample collection and microarray analysis details are described in detail (Arion et al., 2015; Enwright Iii et al., 2017), and the data are publicly available upon request.

22q11DS Patient and Control RNAseq

RNA was extracted from whole blood using the PAXgene extraction kit (Qiagen), then stored at -80C for subsequent analysis. RNA quantity was assessed with Nanodrop (Nanodrop Technologies) and quality with the Agilent Bioanalyzer (Agilent Technologies). Gene expression profiling was performed using Illumina HT-12 v4 microarrays. 200 ng of total RNA were amplified, biotinylated and hybridized to Illumina Human V4-HT-12 Beadchips, including approximately 47,000 probes, following the manufacturer's recommendations. Slides were scanned using Illumina BeadStation, and the signal was extracted by using Illumina BeadStudio software.

Raw data were analyzed using Bioconductor packages in the R statistical environment. Only samples with an RNA integrity number (RIN) of 7 or greater were included in the analyses. Gene expression variance was normalized using variance stabilized transformation. Quality assessment was performed by examining the inter-array biweight midcorrelation; samples more than 3 standard deviations from the mean were excluded. Batch effects were removed using ComBat. Differential gene expression analysis used the *limma* package in R to implement general linear model fit, with batch correction, age, sex, and RIN as covariates.

ATP and ADP Determinations

HAP1 SLC25A1 and SLC25A4 knock-out and the parental control line were grown as described above. On the day of harvest, cells were washed at 37°C twice with pre-warmed PBS. Cells were then scraped up from culture plates in .1M perchloric acid. For *Drosophila*, 10 late third instar larvae or 24-48 h old adults from each genotype were selected and placed into microcentrifuge tubes, flash frozen for 5 min on dry ice and stored at -80°C. The day before

purine analysis, the samples were placed in liquid nitrogen and mechanically crushed using a straight pick awl (Husky #60004H) to break down the cuticle. 400 µL of ice cold .1M perchloric acid was added to each sample and briefly vortexed to mix contents. Cell culture and *Drosophila* samples were kept on ice and sonicated using a (Sonic Dismembrator, Fisher Scientific). 10 µL of 2.5% 3.5M K_2CO_3 was then added to restore pH to 7 or higher and samples stored on ice for 10min. After 10 min, the homogenates were centrifuged at 10,000 rpm for 10 min at 4°C. Supernatant was collected in a 0.45 µm PVDF microcentrifuge filter tube and centrifuged at 10000rpm for 10 minutes at 4°C. Protein pellets and supernatants were flash frozen for 5 min on dry ice and stored at -80°C. Before HPLC analysis, supernatants were slowly thawed on ice. The supernatant was filtered again in 0.22 µm PVDF microcentrifuge filter tubes at 5000 rpm for 5 minutes at 4°C, transferred to Waters Vials with Caps (Waters Corporation 22476) and stored on ice.

Purines were measured by high performance liquid chromatography with photodiode array ultraviolet detection (HPLC-UV). A Waters HPLC system consisting of model 717-plus autosampler, model 1525 binary pump and model 2996 photodiode array detector was used. Analytes were separated using reverse-phase ion-pair chromatography on an Atlantis T3 column (3 µM particle size 4.6 × 150 mm; Waters, Milford, USA). Elution was conducted at 1 ml/min with a stepped gradient of buffer A (10 mM ammonium acetate and 2 mM tetrabutylammonium phosphate, pH 5.0) and buffer B (10 mM ammonium phosphate, 2 mM TBAP, 25% acetonitrile, pH 7.0 before adding acetonitrile). The gradient consistent of the following sequence: 100% buffer A for 10 min; A linear gradient to 75% buffer B over 15 min, 10min at 75% buffer B, a linear gradient to 100% buffer B over 5 min, 100% buffer B for 15min, and a linear gradient to 0% buffer A over 5 min. The column was then re-equilibrated with 100% buffer A for 15min prior to next run. Purines were identified by comparing their retention times and spectral profiles to known standards, quantified at a detection wavelength of 254 nm.

Mitochondrial Ca^{2+} measurements

Mitochondrial Ca^{2+} measurements using the Ca^{2+} sensitive dye Rhod-2/AM (Molecular Probes) were conducted as described (Maxwell et al., 2018). Briefly, Hap1 cells were plated on glass coverslips and loaded with 10 µM Rhod-2/AM with 0.25% Pluronic F-127 (Molecular Probes) in Tyrode's solution for 30 min at room temperature followed by a 30 min de-esterification. Cells were permeabilized with 0.005% saponin to remove the non-mitochondrial Rhod-2 dye. Time-lapse laser scanning confocal microscopy (Olympus FV1000, Melville, NY, USA) was used to image Rhod-2 fluorescence (543 nm excitation/575-675 nm emission). Baseline mitochondrial Ca^{2+} measurements were taken in Ca^{2+}-free internal solution (100 mM Potassium Acetate, 15 mM KCl, 0.35 mM EGTA, 0.75 mM $MgCl_2$, 10 mM HEPES, pH 7.2) and then cells were perfused with internal solution containing 5 µM free Ca^{2+}, calculated using MaxChelator (Bers et al.,

2010). Rhod-2 fluorescence values (F) were normalized to initial fluorescence values (F_0) and plotted as a function of time.

QUANTIFICATION AND STATISTICAL ANALYSIS

Experimental conditions were compared using Synergy Kaleida-Graph, version 4.1.3 (Reading, PA; RRID:SCR_014980) or Aabel NG2 v5 x64 by Gigawiz as specified in each figure. No outlier exclusion was performed.

Results

Genealogical and Comparative Proteomics Prioritize Mitochondrial Targets in 22q11.2 Microdeletions

We quantified proteome differences cosegregating with the 3 Mb microdeletion in 22q11.2 affected human fibroblasts and in brains from mice carrying a syntenic microdeletion in chromosome 16, *Df(16)A+/-*. We used human fibroblasts from pedigrees where one of the individuals was affected by 22q11.2 microdeletion syndrome and childhood psychosis, and compared affected subjects to their disease-free relatives. This strategy, termed genealogical proteomics, minimizes genetic variability between individuals and offers molecular insight into disease mechanisms despite limited subject number (Zlatic et al., 2018). We compared genealogical proteomic outcomes with *Df(16)A+/-* hippocampal and prefrontal cortex proteomes to identify universal mechanisms downstream of the 22q11.2 microdeletion.

We studied proteomes from the following families: one family where all members are disease-free (Fig. 1A), three families harboring one member affected by the 3 Mb 22q11.2 microdeletion (Fig. 1A, E, G), and two isolated 3 Mb 22q11.2 microdeletion patients (Fig. 1A and G). Proteomes were quantified with three mass spectrometry approaches: isobaric tandem mass tagging (TMT, Fig.1B, F), triple SILAC (Fig. 1F, H), and label-free quantification (LFQ, Fig. 1F and Fig. 1-2 supporting Fig. 1). The discriminatory power of genealogical proteomics was tested by comparing the cellular proteomes from 9 individuals within a single multiplexed TMT experiment. These nine individuals are organized in a disease-free family (Fig. 1A, subjects 11-16), a pedigree with one 22q11.2 affected subject (Fig. 1A, subjects 2-3), and an isolated 22q11.2 patient (Fig. 1A, subject 1). Hierarchical clustering of 4264 proteins quantified in all 9 subjects (Fig. 1B) segregated within a cluster all, but one, members of the unaffected family from unrelated subjects (Fig. 1C, subjects 11, 12, 14-16). This dataset contained the quantification of 10 out of the 46 proteins encoded within the 3 Mb 22q11.2 locus (Fig. 1D). Of these proteins SLC25A1, SEPT5, TXNRD2, COMT, RANBP1 and SNAP29 were predictably and significantly reduced by ~50% (Fig. 1D). Thus, genealogical proteomics discriminates genealogical relationships among a limited number of subjects and identifies expected protein expression levels in genes encoded within the 22q11.2 locus. Proteomic analysis of an independent 22q11.2 pedigree using three quantitative mass spectrometry approaches in independent experiments identified partially overlapping proteins whose expression was sensitive to the 22q11.2 microdeletion. However, these three datasets produced convergent and similarly ranked ontology terms (GO CC, see Canvas depiction in Fig. 1-1A and Fig. 1-3 supporting Fig. 1). These results indicate that similar ontological inferences can be obtained from proteomic datasets produced by different quantitation methods, highlighting the rigor and reproducibility of our integrated proteomics approach.

Genealogical proteomics of the three 22q11.2 pedigrees (Fig. 1A-E-G) collectively identified 1500 proteins whose expression was altered in 22q11.2 microdeletion cells (Fig. 1I,

Fig. 1-2 supporting Fig. 1). Of these proteins, only 18 polypeptides were common to all of the 22q11.2 affected individuals (Fig. 1I), including five polypeptides contained in the 22q11.2 locus and 13 polypeptides previously not implicated in 22q11.2 syndrome (Fig. 1I). Independent gene ontology analysis of each one of these three pedigree datasets converged on partially overlapping gene ontology categories (Fig. 1-1B and C and Fig. 1-3 supporting Fig.1). We inferred ontological categories with the 1500 proteins whose expression cosegregated with the 22q11.2 microdeletion, hereafter referred as the 22q11.2 proteome. We used three bioinformatic algorithms which produced similarly ranked ontological categories. We queried the gene ontology cellular component (GO CC), REACTOME, and KEGG pathways simultaneously with the ClueGo algorithm to discern statistically ranked organelles, pathways, and associated pathologies downstream of the 22q11.2 microdeletion (Bindea et al., 2009). The top ontology categories/pathways were all related to mitochondrial compartments (Fig. 2A and Fig. 2-3 supporting Fig. 2, group q value 1.05E-38), as well as diseases where mitochondria are implicated in pathogenesis such as Parkinson's and Huntington's disease (Fig. 2A and Fig. 2-3 supporting Fig. 2, group q value 3.93E-37) (Lin and Beal, 2006). Additionally, the 22q11.2 proteome was enriched in extracellular matrix, lysosome, and actin cytoskeleton components and pathways (Fig. 2A and Fig. 2-3 supporting Fig. 2, group q values 3.23E-23, 6.61E-18, and 7.93E-16, respectively). We confirmed these bioinformatic results with the ENRICHR engine to interrogate the KEGG, OMIM, and GO CC databases (Chen et al., 2013). Mitochondrial compartments and pathways, Parkinson's, Huntington's and other diseases where mitochondria are affected were enriched in the 22q11.2 proteomic dataset (Fig. 2B and Fig. 2-3 supporting Fig. 2, q values 3.3E-36, 1.2E-21, and 5.1 E-12; respectively).

We examined ontology terms inferred from a brain proteome sensitive to the syntenic *Df(16)A+/-* deficiency in mice, hereafter referred as the *Df(16)A+/-* brain proteome (Fig. 2C and Fig. 2-3 supporting Fig. 2). We reasoned that overlapping ontological categories between the 22q11.2 proteome and the *Df(16)A+/-* brain proteome would point to robust and universal mechanisms downstream of the 22q11.2 microdeletion. We profiled by TMT the hippocampus and prefrontal cortex proteomes of control and *Df(16)A+/-* mouse brains. We quantified 6419 proteins and identified 110 hippocampal and 365 prefrontal cortex proteins whose expression was sensitive to the *Df(16)A+/-* microdeletion. ENRICHR bioinformatic analysis indicated that mitochondrial terms were top ranked in the *Df(16)A+/-* hippocampus proteome (Fig. 2C and Fig. 2-3 supporting Fig. 2, q value 0.0018 and combined score of 45.77). In contrast, the spliceosome ranked first in the *Df(16)A+/-* prefrontal cortex proteome (Fig. 2C and Fig. 2-3 supporting Fig. 2, q value 5.01E-06 and combined score of 41.16) with mitochondrial ontological categories scoring in the sixteenth place (Fig. 2C and Fig. 2-3 supporting Fig. 2, p value 0.012 and combined score of 16.52). These ranking differences among ontological hits were due to different mitochondrial polypeptides being affected by the *Df(16)A+/-* microdeletion in the hippocampus and prefrontal cortex mitoproteomes (Fig. 2D-E and Fig. 2-3 supporting Fig. 2).

We attribute these differences to distinctive mitoproteome stoichiometries that distinguish the hippocampus and prefrontal cortex in control mouse brain (Fig. 2F and Fig. 2-4 supporting Fig. 2). These regional mouse brain mitoproteome differences were also observed in flies were distinct neurons of the *Drosophila* mushroom body, the fly hippocampus equivalent (Campbell and Turner, 2010), can be segregated away just based on stoichiometric differences in the transcriptome encoding the fly mitoproteome (Fig. 2-1 supporting Fig. 2) (Chen et al., 2015; Crocker et al., 2016). We conclude that the proteomes sensitive to either the 22q11.2 or the *Df(16)A+/-* hemideficiencies enrich components of the mitoproteome in a brain region-specific manner.

Identification and Prioritization of Key Mitochondrial Proteins within the 22q11.2 Proteome

We used the Mitocarta 2.0 mitoproteome dataset as a reference to identify mitochondrial proteins among the 22q11.2 and *Df(16)A+/-* proteomes (Pagliarini et al., 2008; Calvo et al., 2016). We identified 241 mitochondrial proteins sensitive to the 22q11.2 microdeletion and 48 mitochondrial proteins sensitive to the *Df(16)A+/-* deficiency (Fig. 2G). Expression of fourteen mitochondrial proteins was affected either in all human pedigrees (Fig 1I) or simultaneously in human and mouse cells with the microdeletion (Fig. 2G). We merged these 14 mitochondrial proteins with four additional proteins encoded within the 22q11.2 chromosomal segment which are also part of the Mitocarta 2.0 datasets (Fig. 2G, blue font represents 22q11.2 encoded proteins). A network of protein-protein interactions constrained to these 18 polypeptides was subjected to graph theory analysis to unbiasedly determine node relevance within this network (Fig. 2H). We used clustering, closeness centrality, and betweenness centrality coefficients to measure node relevance (del Rio et al., 2009). The gene products with the highest relevance scores within this interactome were SLC25A1 and SLC25A4 (Fig. 2H). SLC25A1 and SLC25A4 are encoded in the 22q11.2 and 4q35.1 cytogenetic bands. These two transporters participate in central inner mitochondrial solute transport mechanisms and are widely expressed in multiple tissues (Palmieri and Monne, 2016; Taylor, 2017). Thus, we selected these two inner mitochondrial transporters as candidate genes whose disruption would maximize network perturbation.

We confirmed that SLC25A1 and SLC25A4 expression were altered in 22q11.2 fibroblasts as compared to non-affected family members. Both transporters were decreased at least by 50% in 22q11.2 affected fibroblasts as compared to unaffected family members (Fig. 3A, compare lanes 1 and 2, 3-4 and 5, quantified in Fig. 3B). We hypothesized that co-expression changes observed in microdeletion patient cells may be the result of biochemical/metabolic interactions between SLC25A1 and SLC25A4. We used two approaches to address this question. First, we tested whether SLC25A1 and SLC25A4 influenced each other's expression, a common occurrence in proteins that physically interact or belong to a pathway (Wu et al., 2013). We

used cells where SLC25A1 or SLC25A4 expression was abrogated by CRISPR-Cas9 genome editing (Fig. 3C-D). Cells lacking SLC25A1 significantly increased the expression of SLC25A4 ~1.5-2-fold, while SLC25A4-null cells upregulated SLC25A1 3.6 times demonstrating a genetic interaction between these two transporters (Fig. 3C-D). Second, we performed immunomagnetic isolation of SLC25A1 from detergent soluble extracts from wild type and either SLC25A1 or SLC25A4 mutant cells. An SLC25A1 antibody robustly immunoprecipitated a SLC25A1 immunoreactive band absent in SLC25A1 null cells (Fig. 3E compare lanes 3-4). This SLC25A1 antibody also co-immunoprecipitated SLC25A4 from wild type cell extracts but not from SLC25A4 null cells (Fig. 3F compare lanes 3-4). We determined co-precipitation selectivity by blotting for transferrin receptor, a transmembrane protein absent from Mitocarta 2.0 (Fig. 3F, TFRC) (Pagliarini et al., 2008; Calvo et al., 2016). Reverse immunomagnetic isolations with FLAG-tagged SLC25A4 and its paralog SLC25A5 recovered endogenous SLC25A1 (Fig. 3G, lanes 2 and 5). SLC25A1 co-isolation with tagged SLC25A4 and 5 was prevented by FLAG peptide competition (Fig. 3G, lanes 3 and 6). Collectively, these findings demonstrate that SLC25A1 and SLC25A4 genetically and biochemically interact.

Expression of SLC25A Family of Mitochondrial Transporters is Altered in 22q11.2 Fibroblasts and Schizophrenia Patient Neurons

We created a comprehensive *ab initio* SLC25A1-SLC24A4 interactome using as building blocks a SLC25A4-focused interactome plus all SLC25A1 and SLC25A4 interactions curated from seven proteome-wide physical interaction datasets (Fig. 4A and 4-1) (Havugimana et al., 2012; Hein et al., 2015; Huttlin et al., 2015; Wan et al., 2015; Floyd et al., 2016; Huttlin et al., 2017; Lu et al., 2017). The *ab initio* SLC25A1-SLC25A4 interactome contained 106 nodes encompassing mitochondrial respiratory chain components and twelve SLC25A transporter family members (Fig. 4A and 4-1 supporting Fig. 4). The SLC25A1 and SLC25A4 nodes maintained their relative relevance within the *ab initio* network, as ascertained by SLC25A1 and SLC25A4 centrality coefficients (Figs. 4A and 4-1 supporting Fig. 4). Forty five of the 106 *ab initio* SLC25A1-SLC25A4 interactome nodes were represented in the human 22q11.2 proteome indicating a convergence of the 22q11.2 proteome mitochondrial hits and the *ab initio* network (Figs. 4A and 4-1 supporting Fig. 4, grey nodes).

We selected the SLC25A family member transporters to test the reliability of the *ab initio* network (Fig. 4A). We asked whether members of the SLC25A transporter family genetically interacted as inferred from the *ab initio* SLC25A1-SLC25A4 interactome. We first investigated if mRNA levels of SLC25A transporter family members were altered in SLC25A1- or SLC25A4-null cells. We measured transcripts of 10 of the 12 *ab initio* network SLC25A transporters in both SLC25A1 and SLC25A4 knock out cells by qRT-PCR. SLC25A1 null cells significantly altered the expression of 9 of the 10 measured SLC25A transporters while SLC25A4 null cells affected three transporters (Fig. 4B). These changes in transcript content were

selective as evidenced by unaltered levels of the housekeeping genes VAMP3 and VIM (Fig. 4B). We further analyzed if these SLC25A network transporters were affected in other 22q11.2 and syntenic microdeletion tissues. Quantitative mass spectrometry of SLC25A family transporters showed an anticipated decrease of ~50% in SLC25A1 in prefrontal cortex and hippocampus of *Df(16)A+/-* mice (Fig. 4C). Additionally, expression of five out of nine SLC25A family transporters was decreased in prefrontal cortex (Fig. 4C). We extended these observations to lymphoblasts from 77 22q11.2 microdeletion patients and compared mRNA levels to 50 unaffected subjects. Expression of genes within the 22q11.2 locus significantly reduced their expression (Fig. 4D. SNAP29, MRPL40 and SLC25A1). Messenger RNA levels of three out of 10 SLC25A family transporters were significantly reduced in 22q11.2 cells (Fig. 4D). We conclude that components of the *ab initio* SLC25A1-SLC25A4 interactome are affected in tissues from human and mouse carrying 22q11.2 and syntenic microdeletions, respectively. These findings validate the *ab initio* SLC25A1-SLC25A4 interactome for studies of neurodevelopmental and synaptic mechanisms.

We hypothesized that if components of the *ab initio* SLC25A1-SLC25A4 interactome were to participate in the pathogenesis or phenotypic expression of 22q11.2 neuropsychiatric nosology, then neurons from patients affected by schizophrenia or neurons from patients with mutations in the schizophrenia risk gene DISC1 would alter the expression of SLC25A transporters. Expression of SLC25A transcripts was measured by RNAseq in dorsolateral prefrontal cortex gray matter of 57 of age- and sex-matched pairs of unaffected comparison and schizophrenia subjects (Fig. 4E). Of the six SLC25A family transporters with detectable levels of expression, all had mean mRNA levels that were lower in subjects with schizophrenia (Fig. 4E, $q<0.05$ SLC25A3, SLC25A4, SLC25A11, and SLC25A12). Next, pools of layer 3 and layer 5 pyramidal cells and layer 3 parvalbumin cells were individually collected via laser capture microdissection in a subset of subjects (N=36 pairs), and SLC25A transcripts were measured via microarray (Arion et al., 2015; Enwright Iii et al., 2017). Expression of each of the six SLC25A transcripts that were detectable by microarray was lower in all three cell types, though not all met statistical significance (Fig. 4E). The most affected transporter in schizophrenia layer 5 pyramidal neurons was SLC25A4 (Fig. 4E, 30.6% reduction, q value = 0.0222) while in parvalbunim neurons it was SLC25A3 (Fig. 4E, 32.9% reduction, q value = 0.0116). Changes in the expression of SLC25A family transporters was also observed in iPSC-derived human prefrontal neurons carrying a frameshift mutation of DISC1 as compared to isogenic controls generated by editing of the DISC1 gene defect (Wen et al., 2014). Proteomics identified significant changes in the expression of six out of 12 *ab initio* network SLC25A transporters with the most pronounced effects on SLC25A3, SLC25A20, and SLC25A25 (Fig. 4F, q values <0.003), yet the magnitude and direction of these changes were different to those in sporadic cases of schizophrenia (Fig. 4E). These findings are also reproduced in a comprehensive metanalysis of mRNA expression changes in 159 cortical schizophrenia patient samples compared to 293

unaffected subjects (Fig. 4G) (Gandal et al., 2018). These results indicate that components of the *ab initio* SLC25A1-SLC25A4 interactome are altered in tissue samples from patients affected by neurodevelopmental disorders sharing phenotypes with the 22q11.2 syndrome. Collectively, these findings demonstrate that SLC25A1 and SLC25A4 are principal nodes within a mitochondrial interactome. Our results suggest that partial down-regulation of these mitochondrial transporters and their interactome may participate in mechanisms necessary for synapse function and behavior.

SLC25A1 and SLC25A4 are required for normal synapse development and to maintain the synaptic mitochondrial pool.

To test the consequences of a partial decrease in the expression of SLC25A mitochondrial transporters on neuronal function and behavior, we selected *Drosophila* because of genetic tools that allow precise control of gene expression in a developmental-, cell-, and tissue-restricted fashion. We focused on studying synaptic and behavioral phenotypes caused by SLC25A1 and SLC25A4 haploinsufficiencies in *Drosophila*. SLC25A1 and SLC25A4 orthologues are encoded by the gene *scheggia* (*sea*, CG6782, dSLC25A1) and *stress-sensitive B* genes (*sesB*, CG16944, dSLC25A4), respectively. We examined morphological and electrophysiological phenotypes in the third instar *Drosophila* neuromuscular junction synapse, which is a reliable model to assess synaptic developmental phenotypes associated with neurodevelopmental gene defects (Frank et al., 2013). We controlled the expression of dSLC25A1-sea with UAS-RNAi reagents and the null allele $sea^{\Delta 24}$ (Morciano et al., 2009). dSLC25A4-sesB expression was modified with UAS-RNAi as well as two genomic alleles of *sesB*, $sesB^{org}$ and $sesB^{9Ed\text{-}1}$. $sesB^{org}$ is a thermosensitive allele that decreases the ADP-ATP transport activity by 60%, offering a functional haploinsufficiency model (Rikhy et al., 2003). In contrast, $sesB^{9Ed\text{-}1}$ is a strong lethal null allele that is viable as single copy deficiency (Zhang et al., 1999). We confirmed that *UAS-sea* or *UAS-sesB* RNAi transgenes driven by actin-GAL4 indeed reduced mRNA expression of their target genes by 50% in *Drosophila* heads (Fig. 8C). Therefore, these fly reagents mimic the partial reduction in the expression of SLC25A family members observed in 22q11.2 human and mouse mutant tissues, as well as samples from patients diagnosed with schizophrenia (Fig. 3 and 4).

We used genomic alleles and RNAi transgenes driven by neuronal specific $elav^{c155}$*-Gal4* and *VGlut-Gal4* transgenic drivers and analyzed the morphology of the larval neuromuscular junction (Fig. 5). Reducing the expression of sea or sesB by half increased the number of boutons and/or branches per synapse, irrespective of whether genomic alleles or neuronal specific RNAi decreased transporter expression (Fig. 5A-B). These synaptic morphological phenotypes could be simply attributed to reduced mitochondrial function caused by these haploinsuffiencies. We scrutinized this hypothesis by genetic and biochemical approaches. First, we compared outcomes of single or double neuronal-specific dSLC25A1 and dSLC25A4 RNAi on

synapse morphology. If reduced mitochondrial function accounts for phenotypes observed in single transporter genetic defects, we reasoned that combined RNAi of these two transporters should enhance synaptic morphological phenotypes as compare to single RNAi synapses. Contrary to this prediction, double dSLC25A1-sea plus dSLC25A4-sesB RNAi rescued synapse morphology (Fig. 5A-B). Second, we measured ATP/ADP ratios in *Drosophila* dSLC25A1-sea and dSLC25A4-sesB RNAi haploinsufficient larvae and *Drosophila* heads (Fig. 5-1 supporting Fig. 5). ATP/ADP ratios were not significantly and predictably modified in both tissues. The same is the case in mutant human SLC25A1 cells, even though the mutation completely abrogated SLC25A1 expression (Fig. 3C-D and Fig. 5-1 supporting Fig. 5). However, the ATP/ADP ratio was decreased by half in SLC25A4 null human cells (Fig. 5-1 supporting Fig. 5). This last result is expected and confirms the sensitivity of our assay (Klingenberg, 2008). These genetic and biochemical findings strongly argue against loss of mitochondrial function caused by dSLC25A1-sea or dSLC25A4-sesB RNAi haploinsufficiencies.

Mutations in the GTPase miro deplete synapses from mitochondria and increase the number of boutons at the *Drosophila* neuromuscular synapse (Guo et al., 2005). Moreover, mutations in miro and Drp1 that severely deplete synaptic mitochondria also selectively compromise neurotransmission at high frequencies while sparing the amplitude of evoked and spontaneous neurotransmission events (Guo et al., 2005; Verstreken et al., 2005). This prompted us to ask if the increased synaptic branching in dSLC25A1-sea or dSLC25A4-sesB haploinsufficiencies could be associated to synaptic mitochondrial depletion and impaired high frequency neurotransmission. We quantified mitochondria in larval neuromuscular junctions by neuronally expressing a UAS-mitochondria-GFP transgene in animals harboring either UAS-sea or UAS-sesB RNAi transgenes. Down-regulation of dSLC25A1-sea increases mitochondrial content at the synapse 1.8 times while down-regulation of dSLC25A4-sesB decreases mitochondrial content by half (Fig. 6). These results demonstrate that dSLC25A1-sea and dSLC25A4-sesB are required to maintain the synaptic pool of mitochondria and exclude mitochondrial depletion as a cause of the synapse branching phenotype.

We next asked whether the partial reduction in mitochondrial content in dSLC25A4-*sesB* haploinsufficient synapses was consequential for neurotransmission. Evoked neurotransmission, measured as evoked excitatory junction potential amplitude (EJP) (Fig. 7A and C, and Fig. 8A-B), and spontaneous miniature excitatory junction potential amplitude (mEJP) (Fig. 7B and D, and Fig. 8D-E), remained unaffected in all *sesB* genotypes tested. We examined and compared neurotransmission elicited at 3Hz and at high frequency (10Hz) on wild type and *sesB* haploinsufficient synapses (Fig. 7E-K). We incubated neuromuscular junctions in the presence of bafilomycin A1, a vacuolar ATPase inhibitor, to prevent neurotransmitter vesicle reloading after a round of vesicle fusion (Delgado et al., 2000; Kim et al., 2009; Mullin et al., 2015). This strategy leads to synapse fatigue in wild type larvae due to synaptic vesicle depletion (Fig. 7E-H, gray curves). Synaptic transmission at low frequency

stimulation was normal in *sesB* deficient synapses (Fig. 7E, I, K). However, neurotransmission at high frequency was consistently increased in all *sesB* alleles as expressed by synaptic resilience to fatigue (10Hz, Fig. 7F-G, J, K). These effects were due to changes in the expression of sesB in neurons and not the muscle, as demonstrated by down-regulation of sesB with neuronal-specific RNAi (Fig. 7H, J, K). These results demonstrate that dSLC25A1-sea and dSLC25A4-sesB haploinsufficiencies differentially control the synaptic pool of mitochondria, irrespective of the synaptic bouton count, and in the case of dSLC25A4-*sesB*, without impairing high frequency neurotransmission.

SLC25A1 and SLC25A4 differentially modulate calcium-dependent synaptic activity.

Calcium and mitochondrial calcium stores modulate spontaneous and evoked synaptic transmission as well as synaptic plasticity (Vos et al., 2010). To determine if dSLC25A1-sea and dSLC25A4-sesB haploinsufficiencies affect mitochondrial calcium storage, we measured the message levels of calcium pumps and transporters residing in mitochondria and endoplasmic reticulum, spontaneous and evoked neurotransmission, and paired-pulse facilitation at low and high extracellular calcium. We chose paired-pulse facilitation because its sensitivity to the functional integrity of mitochondrial (Weeber et al., 2002; Levy et al., 2003; Regehr, 2012).

We first sought to established whether complete knock-out of any of these SLC25A transporters could compromise mitochondrial calcium buffering mechanisms. We used human cells rendered SLC25A1- or SLC25A4-null by CRISPR-Cas9 genome editing. Mitochondria were labeled with the Ca^{2+}-sensitive dye Rhod-2/AM, followed by perfusion with a calcium-containing buffer. Wild type mitochondrial rapidly increased their fluorescence (Fig. 8A). In contrast, the calcium influx rate was similarly reduced in either SLC25A1- or SLC25A4-null mitochondria to ~50% (Fig. 8A-B). Expression of the mitochondrial calcium uniporter (MCU) and endoplasmic reticulum calcium ATPases (SERCA1-3) mRNAs was unaltered in both null cells (data not shown). These results raise the possibility that dSLC25A1-sea and dSLC25A4-sesB haploinsufficiencies may modulate calcium-dependent neurotransmission and plasticity.

The expression of the mitochondrial calcium uniporter (MCU) and the endoplasmic reticulum calcium ATPase (SERCA) mRNAs was normal in dSLC25A1-sea and dSLC25A4-sesB haploinsufficient *Drosophila* heads (Fig. 8C). Thus, we inquired whether dSLC25A1-sea and dSLC25A4-sesB haploinsufficiencies could affect spontaneous neurotransmission in a calcium-sensitive manner (Fig. 8D-F). The amplitude of spontaneous fusion events (mEJPs) was neither altered by dSLC25A1-sea nor dSLC25A4-sesB haploinsufficiency, nor by the extracellular calcium concentration (Fig. 8D-E). However, the frequency of the mEJPs was increased in $sea^{\Delta 24}$/+ synapses both at low and high extracellular calcium while $sesB^{org}$/+ synapses increased their frequency only at high calcium concentrations (Fig. 8D and F). These results suggest an impaired calcium buffering capacity at haploinsufficient synapses. These different mEJP frequency responses between dSLC25A1-*sea* and dSLC25A4-*sesB* haploinsufficiencies could reflect the

same mechanism affected to a different extent or divergent calcium buffering mechanisms affected by dSLC25A1-*sea* and dSLC25A4-*sesB*. To resolve between these hypotheses, we analyzed paired-pulsed facilitation (Fig. 8G-I). We reasoned that paired-pulsed facilitation should be similarly perturbed in $sea^{\Delta 24}$/+ and $sesB^{org}$/+ synapses under a common mechanism model. $sesB^{org}$/+ synapses have reduced paired-pulsed facilitation at low extracellular calcium concentrations but normal at high extracellular calcium (Fig. 8G and I). In contrast, paired-pulsed facilitation was normal at both extracellular calcium concentrations in $sea^{\Delta 24}$/+ synapses (Fig. 8G and I). These results support a model whereby different calcium buffering mechanisms are perturbed in dSLC25A1-*sea* and dSLC25A4-*sesB* heterozygotic synapses.

SLC25A1 and SLC25A4 haploinsufficiencies differentially modulate behavior

To assess the behavioral consequences of partial loss of function in components of the SLC25A1-SLC25A4 interactome, we analyzed sleep patterns in wild type animals and mutants carrying $sesB^{org}$, $sesB^{9Ed-1}$, and *sesB* RNAi (Fig. 9). We contrasted *sesB*-dependent phenotypes with sleep phenotypes induced by down-regulation of dSLC25A1-sea (Fig. 9-1 supporting Fig. 9). We chose sleep as a non-invasive and high throughput analysis of an adult behavior which is entrained by environmental cues (Hendricks et al., 2000; Freeman et al., 2012). Moreover, sleep alterations are frequent in neurodevelopmental disorders (Chouinard et al., 2004; Monti and Monti, 2004; Krakowiak et al., 2008; Petrovsky et al., 2014; Kamath et al., 2015). We measured locomotor activity using the *Drosophila* Activity Monitoring (DAM) system to quantify episodes of activity and sleep in a 12:12 hour light:dark cycle. Wild type Canton S animals demonstrated the highest density of sleep activity during the dark period (Fig. 9A-B and Fig. 9-1 supporting Fig. 9, zeitgeber times ZT12 to 24) with an increased number of sleep-wake transitions at the beginning and end of the light cycle (Fig. 9A-B and Fig. 9-1 supporting Fig. 9, zeitgeber times ZT1 and 12). This pattern was disrupted in $sesB^{org}$ and $sesB^{9Ed-1}$ animals, which exhibit increased sleep-wake transitions throughout the 24-hour period (Fig. 9A-B, zeitgeber times ZT1 to 24). Most sleep events occurred at night (Fig. 9A-B and Fig. 9-1 supporting Fig. 9, zeitgeber times ZT12 to 24). This pattern was disrupted in $sesB^{org}$ and $sesB^{9Ed-1}$ animals, which experienced increased awake-sleep transitions throughout the whole day (Fig. 9A-B, zeitgeber times ZT1 to 24). *sesB* deficient animals slept more (Fig. 9C-D and G), a phenotype that was evident during the day (Fig. 9A-B, zeitgeber times ZT1 to 12 and Fig 7E) and night (Fig. 9A-B, zeitgeber times ZT12 to 24 and Fig. 9F). The sleep increase phenotype observed in *sesB* alleles was selectively phenocopied only by glutamatergic neuron-specific sesB RNAi (Fig. 9H, Vglut driver). Neither glial-specific (Fig. 9I, repo driver) nor dopaminergic neuron-specific sesB RNAi elicited any sleep phenotypes (Fig. 9J, Ddc driver). These *sesB*-dependent phenotypes were in sharp contrast with the *sea*-dependent traits in two key aspects. First, sea RNAi decreased, rather than increased, total sleep duration, but only during the light period (Fig. 9-1A-B supporting Fig. 9, zeitgeber times ZT1 to 12 and compare Fig. 9-1C-D with E-F). Second, this

light-selective phenotype was only induced by downregulation of dSLC25A1-sea in dopaminergic neurons but not in glutamatergic neurons (Fig. 9-1 supporting Fig. 9 compare C-D with I-J). These results demonstrate that partial loss of function in dSLC25A1-sea or dSLC25A4-sesB produce neuronal-cell type specific alterations of sleep.

Collectively, our findings demonstrate that synaptic morphology, plasticity, and complex behaviors are sensitive to partial loss of function of mitochondrial solute transporters. We propose that cell-type specific mitoproteomes tune synapse development and function in normal and disease states.

Discussion

We identified mitochondrial pathways as statistically prioritized ontological terms in the 22q11.2 and the *Df(16)A+/-* proteomes. Our results recapitulate a previous proteomic study of *Df(16)A+/-* brains which is also enriched in mitochondrial targets (Fig. 2-2 supporting Fig. 2) (Wesseling et al., 2017). Here, we expanded this prior study by demonstrating first, that mitoproteomes are affected in neuronal and non-neuronal cells carrying this microdeletion. Second, we identified a novel interaction between the inner mitochondrial transporters SLC25A1 and SLC25A4; this physical, functional, and genetic interaction forming a high connectivity hub downstream to the 22q11.2 microdeletion (Fig. 4A and 4-1). The proper gene dosage of these mitochondrial transporters is required for normal synapse morphology, function, plasticity and behavior as demonstrated by *Drosophila* haploinsufficiencies in dSLC25A1-sea and dSLC25A4-*sesB* (Figs. 5 to 9). We further curated a SLC25A1-SLC25A4 interactome using comprehensive *in silico* tools and found that the expression of other SLC25A transporters belonging to this interactome is altered in neurons from schizophrenia cases where the genetic risk factor is other than the 22q11.2 microdeletion (Fig. 4E-G). Our systems analysis of the 22q11.2 and the *Df(16)A+/-* proteomes intersects with studies where changes in mitochondrial ontologies strongly associate with psychiatric disease (Gandal et al., 2018) and with reports of alterations in mitochondrial transcripts, protein composition, function, and morphology in brains from patients with psychotic disorders (Middleton et al., 2002; Rosenfeld et al., 2011; Enwright Iii et al., 2017; Norkett et al., 2017). While our studies were carried out in a single *Drosophila* peripheral synapse and await confirmation in mammalian central synapses; our results support the hypothesis that the mitochondrion, in particular components of the SLC25A1-SLC25A4 interactome (Fig. 4A and 4-1), modulate the risk of neurodevelopmental disorders.

The robustness of our gene ontology conclusions is founded on the strong agreement between the 22q11.2 and the *Df(16)A+/-* proteomes. However, we deem necessary to discuss limitations inherent to the genealogical proteomic approach used here to generate the 22q11.2 proteome. First, the use of fibroblasts limits proteomic surveys to uncover systemic rather than neuronal-specific molecular phenotypes. Second, we observed that gene ontologies derived from different families are not overlapping despite the consistency of ontologies obtained from the same family yet with different quantitative proteomics methods (Fig. 1-1 supporting Fig. 1). Although we minimized the noise introduced by genetic variability among subjects by comparing proteomes within a family; noise introduced by variables like age, sex, cell passage, and epigenetic modifications due to possible drug use still contribute to our datasets. To circumvent these limitations, we reasoned that if 22q11.2 proteomes from different families contained a majority of 22q11.2-specific hits plus different sources of random noise, then the addition of these family-specific proteomes into one dataset should enrich 22q11.2-specific gene ontologies while degrading ontologies due to random noise. We empirically tested this

idea by adding the 22q11.2 and the *Df(16)A+/-* proteomes, which resulted in improved statistical scores for the ontological categories associated to each one of these two datasets while maintaining their overall priority rank (Fig. 2-2C supporting Fig. 2). In contrast, addition of a random gene dataset of increasing size progressively degraded statistical scores and/or ranking of microdeletion-specific ontological categories (Fig. 2-2C supporting Fig. 2). These *in silico* data analyses support our approach of adding 22q11.2 family-specific proteomes to enrich gene ontologies affected by a genetic defect while diluting those generated by random noise. However, the best evidence supporting genealogical proteomics are the two independent *Df(16)A+/-* brain proteomes which validate our studies (Fig. 2 and 2-2). All three datasets, one in human and two in mouse, converge on similar ontological categories and rankings despite differences in tissues, species, and proteomic platforms used. The use of isogenic model systems is a way to circumvent random noise introduced by limited number of families in genealogical proteomics. Alternatively, either increasing the number of families analyzed or using different biological samples from the same family (fibroblasts, lymphoblasts, and IPSCs) should minimize the effects of noise on a dataset due to unforeseen variables or independent variables out of experimental reach.

The 22q11.2 locus encodes seven proteins contained in the Mitocarta 2.0 mitoproteome (COMT, MRPL40, PI4K, PRODH, SLC25A1, SNAP29, and TXNRD2) (Pagliarini et al., 2008; Calvo et al., 2016). Some of these loci have been documented or proposed to be required for normal synaptic function (Paterlini et al., 2005; Maynard et al., 2008; Crabtree et al., 2016; Devaraju et al., 2017). The mitoproteome of 22q11.2 mutant cells and *Df(16)A+/-* brain likely reflect the collective effect of some or all these seven hemideficient genes (Devaraju et al., 2017; Devaraju and Zakharenko, 2017). We argue that these seven genes may not be the only 22q11.2 loci contributing to the alterations in the mitoproteome. For example, the DGCR8 gene, controlling microRNA-production, and seven miRNAs present in the 22q11.2 chromosomal segment could modulate the mitochondrial proteome acting both in nuclear and mitochondrial encoded RNAs (Stark et al., 2008; Chan et al., 2009; Bandiera et al., 2011; Minones-Moyano et al., 2011; Zhang et al., 2014). The seven 22q11.2 genes which are part of Mitocarta 2.0 are differentially expressed in different brain regions and cell types. Thus, their expression could influence the extent and quality of changes in mitochondrial proteomes from different cell types and brain regions in normal and disease states. We found that the stoichiometry of the mitoproteome or mitotranscriptome is different between two brain regions in normal mouse brain and between different cell types within *Drosophila* mushroom bodies (Fig. 2 and 2-1 supporting Fig. 2). We believe these regional and cellular differences in mitochondrial composition stoichiometry are consequential as the impact of dSLC25A1-sea or dSLC25A4-sesB haploinsufficiencies on *Drosophila* neurotransmission, synaptic plasticity, sleep patterns is differential. The clearest example is the disruption of sleep by dSLC25A1-sea or dSLC25A4-sesB haploinsufficiencies, where a phenotype depends on whether glutamatergic or catecholaminergic cells are targeted.

It remains to be confirmed whether these effects are phenocopied by cell type-specific downregulation or knock-out of other components of the SLC25A1-SLC25A4 interactome in vertebrate and invertebrate brains. However, it is reasonable to propose that differences in mitochondrial composition stoichiometry in different neuronal cell types could explain why, of the SLC25A transcripts analyzed, SLC25A3 was the most affected in layer 3 parvalbumin cells and SLC25A4 the most affected in layers 3 and 5 pyramidal cells in subjects with schizophrenia (Fig. 4E).

22q11.2 microdeletion syndrome increases the risk of developing schizophrenia or Parkinson's disease by 20-fold (Bassett et al., 2000; Hodgkinson et al., 2001; Bassett and Chow, 2008; Zaleski et al., 2009; Butcher et al., 2013; Mok et al., 2016; Butcher et al., 2017). This observation prompted us to ask about the identity of candidate pathways capable of contributing to both psychiatric and neurodegenerative phenotypes. Complex I and other respiratory complex subunits are prominently represented in the 22q11.2 and *Df(16)A+/-* proteomes and the SLC25A1-SLC25A4 interactome (Figs. 4 and 4-1). Respiratory chain complexes could contribute to the expression of psychiatric and/or neurodegenerative pathologies. Our contention is founded on the capacity of complex I chemical inhibitors to either cause Parkinson's-like phenotypes (MPP+ and rotenone) or ameliorate psychosis symptoms (haloperidol, chlorpromazine, risperidone) (Burkhardt et al., 1993; Prince et al., 1997; Modica-Napolitano et al., 2003; Rosenfeld et al., 2011; Elmorsy and Smith, 2015). Moreover, primarily mitochondrial diseases that affect the activity of the respiratory chain complexes, such as Leigh syndrome, can cause neurodegeneration and psychiatric symptoms (DiMauro and Schon, 2008; Anglin et al., 2012b; Anglin et al., 2012a; Sheng and Cai, 2012). While still speculative, we put forward a testable model where changes in the expression of the mitoproteome modulate the expression of neurodevelopmental and/or neurodegenerative phenotypes.

Acknowledgements

This work was supported by grants from the National Institutes of Health R56 MH111459 to VF and Emory Catalyst Grant, Fondecyt-Chile grant 1171014 to GMR, R01HL108882 to SMC, R01MH097879 to JAG. CH is supported by the FIRST postdoctoral fellowship NIH 5K12GM000680. We thank members of the Faundez Lab for their comments and insight. Stocks obtained from the Bloomington *Drosophila* Stock Center (NIH P40OD018537) were used in this study. This study was supported in part by the Emory HPLC Bioanalytical Core (EHBC) and the Emory Imaging Core. EHBC is supported by the Department of Pharmacology, Emory University School of Medicine and the Georgia Clinical & Translational Science Alliance of the National Institutes of Health under Award Number UL1TR002378.

Declaration of Interests

There are no interests to declare by all authors

Figure Legends

Fig. 1. Genealogical Proteomics of 22q11.2 Pedigrees Fibroblasts Using Quantitative Mass Spectrometry.

Human pedigrees of a control family (A) and families where one of the subjects is affected by 22q11.2 microdeletion syndrome and early childhood psychosis (blue numbers in A, E, G). Experimental design is designated at the upper left corner of dot plots (B, F, H). For example, (B) shows a TMT experiment where proteomes from probands 1 and 2 were compared against unaffected individuals 3, 11-16. C) Hierarchical clustering analysis of the proteome in subjects 1-3 and 11-16. Euclidian distance clustering of columns and rows (4264 TMT protein quantitations) shows segregation of related family members. D) Dot plot of proteins encoded within the 22q11.2 chromosomal segment quantitated in TMT experiment B. Asterisks denotes significant differences p= 0.04146 to p<0.0001 T-test. B, F and H depict all mass spectrometry quantifications where the color code denotes individuals being compared (blue symbols are proteins whose expression is changed, grey symbols are unaffected proteins). Significant protein expression changes for: TMT and SILAC were consider to be >2 or <0.5 whereas in label free quantification (LFQ) a -log(p) value threshold of 1.3 was used. I) Venn diagram summarizes proteins with significant expression changes in B, F and H. Asterisk denotes proteins whose expression changed in all patients. Bold font depicts proteins encoded within the 22q11.2 segment. Blue color fonts are proteins contained in the human Mitocarta 2.0 dataset. Individual MS/MS data can be found in Fig.1-2. Ontological comparisons among pedigrees and proteomic platforms can be found in Fig. 1-1 and 1-3.

Fig. 1-1. 22q11.2 Microdeletion Genealogical Proteome Comparisons Among Pedigrees and Mass Spectrometry Quantitation Strategies. A-D) Cellular Component Gene ontologies (GO:CC) obtained using the ENRICHR engine. Data are depicted as canvases where every tile is occupied by an individual GO category whose p value significance is depicted by color intensity. A) First canvas to the left depicts a comparison for genealogical proteomes obtained in one pedigree by TMT (green) and to Label Free Quantification (LFQ, red). Other canvases in A show experiments comparing TMT with two independent SILAC experiments and combinations of TMT, LFQ and SILAC. Overlap of GO:CC terms is presented as yellow. B) Comparison of GO:CC terms obtained by genealogical proteomics from three pedigrees. C) Represents GO:CC term tiles overlapping among pedigrees in B). D) Shows gene ontology terms obtained by pooling into one dataset the proteomes from all pedigrees in B). E. Presents relevant GO terms in D. Individual pedigree and collective bioinformatics data can be found in Fig. 1-3.

Fig. 1-2. Quantitative Mass Spectrometry Data for 22q11.2 Genealogical Proteomic Studies.

Fig.1-3. Comparative Bioinformatic Analysis of 22q11.2 Genealogical Proteomes.

Fig. 2. Comparative Bioinformatic Analysis of the 22q11.2 and the *Df(16)A+/-* Mouse Brain Proteomes.

A) The 22q11.2 Proteome was analyzed with the engine ClueGo integrating the Cellular Component gene ontology GO:CC, REACTOME and KEGG databases. Functionally grouped network was built with terms as nodes and edges based on their term-term similarity statistics. The node size represents the term enrichment significance ($p < 0.015$ Bonferroni corrected). B) ENRICHR analysis of the 22q11.2 Proteome querying GO CC, KEEG and OMIM databases. C) ENRICHR analysis of the *Df(16)A+/-* mouse hippocampus and prefrontal cortex (PFC) proteomes as in B. Mouse brain proteomes were quantified using TMT mass spectrometry (see Fig. 2-4, n= 6 mutant and 5 control mice). D-F) Differences in the mitoproteomes of wild type and *Df(16)A+/-* mitoproteomes. Hierarchical clustering analysis of the *Df(16)A+/-* mouse hippocampus and prefrontal cortex mitochondrial proteome hits (D-E) is compared to the wild type mitoproteomes quantified in hippocampus (Hipp) and prefrontal cortex (PFC). Kendall's tau distance clustering of columns and rows. In E, the asterisk marks a wild type animal. Fig. 2-1 presents a similar analysis of mitochondrial transcriptomes in different *Drosophila* neurons. G) Venn diagrams present overlapping protein hits between the 22q11.2 and *Df(16)A+/-* proteome with the human and mouse Mitocarta 2.0 datasets. Listed proteins correspond to mitochondrial proteins whose expression is sensitive to the microdeletion in human and mouse (upper two columns). Lower column and blue font proteins are encoded in the 22q11.2 chromosomal segment. Comparisons with previous *Df(16)A+/-* proteome are depicted in Fig. 2-2. H) SLC25A1 and SLC25A4 are high connectivity nodes in a discrete 22q11.2 and *Df(16)A+/-* mitoproteome interactome. In silico interactome of protein hits listed in G. Interactome was analyzed with graph theory to determine high connectivity nodes predictive of essential genes. Additional bioinformatic data and MS/MS data can be found in Figs. 2-3 and 2-4.

Fig. 2-1. The Drosophila Transcriptome Encoding Mitochondrial Proteins is Cell Type Specific. A-B) mRNA from single neuron types isolated from *Drosophila* mushroom bodies were analyzed by RNAseq. The transcriptome encoding mitochondrial proteins, as defined by Chen et al (Chen et al., 2015), was analyzed by principal component analysis (A) and hierarchical clustering using 1-Pearson correlation clustering (B) of columns (cells) and rows (transcripts). Cell types were identified as in Crocker et al (Crocker et al., 2016). Note the robust segregation of Kenyon cells from other cell types by the expression of the transcriptome encoding mitochondrial proteins.

Fig. 2-2. Comparative Bioinformatics of the 22q11.2 Proteome and Two Independent *Df(16)A-/+* Brain Proteomes.

A) Venn diagrams depict from top to bottom: a comparison of common hits between our *Df(16)A-/+* brain proteome and the *Df(16)A-/+* brain proteome reported by Wesseling et al. PMID: 27001617. The Wesseling *Df(16)A-/+* brain proteome and our 22q11.2 proteome. The

Wesseling *Df(16)A*-/+ brain proteome and the mouse Mitocarta 2.0 dataset. B) Cellular Component gene ontology analysis of GO CC generated with the ENRICHR engine using the Wesseling *Df(16)A*-/+ brain proteome dataset and a similarly sized random mouse gene dataset. Random gene list was generated with the engine RandomGeneSetGenerator. C) Cellular Component gene ontology analysis (GO CC) was performed with the ENRICHR engine using the Wesseling *Df(16)A*-/+ brain proteome dataset either by itself, or in combination with our 22q11.2 proteome, or with 1500 (1x) or 3000 (2x) randomly generated genes. See discussion.

Fig. 2-3. Bioinformatic Analysis of 22q11.2 Genealogical Proteomes and *Df(16)A*-/+ brain proteomes.

Fig. 2-4. Quantitative Mass Spectrometry Data for *Df(16)A*-/+ brains.

Fig. 3. SLC25A1 and SLC25A4 Expression is Affected by the 22q11.2 Microdeletion Cell and these transporters Biochemically and Genetically Interact.

A) Human pedigrees of families affected by 22q11.2 microdeletion syndrome. Immunoblots of total cellular lysates from fibroblasts obtained from individuals in pedigrees. B) Quantitation of results shown in A. p values One way ANOVA followed by Dunnett's multiple comparisons, n=3. C) SLC25A1 and SLC25A4 expression changes in cells carrying null mutations (Δ) in *SLC25A1* or *SLC25A4* clonal cell lines. Detergent soluble cell extracts were blotted with indicated antibodies. Actin (ACTB) and HSP90 were used as controls. D) Depicts quantitation of expression levels as compared to wild type cells. p values One way ANOVA followed by Dunnett's multiple comparisons, n=5. E) SLC25A1 antibody precipitates an SLC25A1 immunoreactive band (lane 3) absent from SLC25A1 null cells (lane 4). Asterisks denote non-specific bands recognized by the antibody. F) SLC25A1 antibody precipitates an SLC25A4 immunoreactive band (lane 3) absent from SLC25A4 null cells (lane 4). G) FLAG tagged SLC25A4 or SLC25A5 precipitate SLC25A1 (lames 2 and 5). Lanes 1 and 3 correspond to inputs. Lanes 4 and 6 correspond to immunoprecipitation where an excess FLAG peptide was used for outcompetition. F-G) Transferrin receptor (TFRC) was used as a control for non-specific membrane protein precipitation.

Fig. 4. Expression of Components of the SLC25A1-SLC25A4 Interactome is Affected in Neurodevelopmental Disorders.

A) Comprehensive *in silico* interactome of the SLC25A1 and SLC25A4 mitochondrial transporters. Complexes I to V of the respiratory chain as well as SLC25A transporter family members are color coded. All nodes colored gray represents hits in the 22q11.2 proteome. Additional details can be found in Fig. 4-1. B) Expression of SLC25A transporter family member transcripts is altered in SLC25A1 or SLC25A4 null cells. Transcript quantification by qRT-PCR is

expressed as ratio to vimentin mRNA. VAMP3 was used as control. n=4 One Way ANOVA followed by Fisher's Least Significant Difference Comparison. All non-significant comparisons are marked (NS). C) Expression of SLC25A transporter family member polypeptides is altered in *Df(16)A+/-* mouse hippocampus (Hipp) or prefrontal cortex (PFC). SLC25A transporters were quantitated by TMT mass spectrometry. n= 6 mutant and 5 control mice. One Way ANOVA followed by Fisher's Least Significant Difference Comparison. Asterisk marks p≤0.0001. ** p=0.0098, *** p≤0.028. D) Expression of SLC25A family member mRNAs is reduced in whole blood from unaffected and 22q11.2 patients. Probability plots of mRNA quantified by microarray on 50 unaffected (grey) and 77 22q11.2 patients (blue). SNAP29, MRPL40 and SLC25A1 reside in the 22q11.2 microdeletion locus and were used as controls to determine the range of expression change attributable to the microdeletion. SLC25A3 and SLC25A25 expression is modified within this range. P values were calculated using Kolmogorov–Smirnov test. E) mRNA expression of SLC25A transporters in gray matter or single cells isolated from unaffected and schizophrenia cases. Gray matter mRNA quantitations were performed by RNAseq while single cell mRNA quantitations were performed by microarray in dorsolateral prefrontal cortex (DLPFC) samples. F) Proteomic quantitation of SLC25A transporters in iPSC-derived cortical neurons from DISC-1 mutant patient and isogenic controls. E-F) SLC25A transporter family members SLC25An where n correspond to the number on blue circle. Grey box denotes non-significant changes in expression after multiple corrections. G) mRNA expression of SLC25A transporter family members is altered in schizophrenia brains. Meta-analysis data obtained from Gandal et al. (Gandal et al., 2018).

Fig. 4-1. Comprehensive *in silico* Interactome of the SLC25A1 and SLC25A4 Transporters.

A) Comprehensive *in silico* interactome of the SLC25A1 and SLC25A4 mitochondrial transporters. Complexes I to V of the respiratory chain as well as SLC25A transporter family members are color coded. All nodes colored gray represent hits in the 22q11.2 proteome. B) The comprehensive interactome was analyzed with graph theory to determine high connectivity nodes predictive of essential genes using the closeness and betweeness centrality coefficients. Note the high connectivity of SLC25A4 in the comprehensive interactome.

Fig. 5. Reduced Expression of *Drosophila* dSLC25A1-dSLC25A4 Alters Synapse Morphology.

A and B) Muscle VI-VII third instar neuromuscular junctions were stained with antibodies against the neuronal marker HRP. Expression of SLC25A1 (*sea*, *scheggia*) was downregulated with two RNAi transgenes or the null allele $sea^{\Delta 24}$/+. dSLC24A4 expression was reduced with a RNAi transgene or two genomic alleles ($sesB^{org}$ and $sesB^{9Ed\text{-}1/+}$). Neuronal specific expression of RNAi regents was driven by the $elav^{c155}$-GAL4 (*c155*) or *Vglut*-GAL4 drivers.

w1118, w1118; *elav*^{c155}-GAL4 or w1118; *Vglut*-GAL4 animals were used as controls. B) Shows quantitation of bouton counts per synapse. Counts were performed blind to the animal genotype. All comparisons in B were performed with One-Way ANOVA followed by Bonferroni's multiple comparison. Number of animals is at the bottom of each box. Analysis of ATP/ADP ratios in tissues from mutant animals can be found in Fig. 5-1.

Fig. 5-1. Reduced Expression of *Drosophila* dSLC25A1-dSLC25A4 does not Affect Cellular ATP/ADP ratios.

ATP/ADP ratios were measured in third instar larvae, adult heads, and human Hap1 cells of the indicated genotypes. n=3 for Drosophila Tissues and n=6 for Hap1 cells, One Way ANOVA followed by Fisher's Least Significant Difference Comparison.

Fig. 6. *Drosophila* SLC25A1-sea and SLC25A4-sesB are Required for Mantaining the Synapse Mitochodrial Pool.

Triple-stained muscle VI-VII third instar neuromuscular junctions from *elav*^{c155}-GAL4;w1118 wild type larvae (n=8) or *elav*^{c155}-GAL4 crossed to either *sea*$^{\Delta 24}$/+ (n=8) or *sesB*$^{Org/+}$ (n=7) were imaged by confocal microscopy. Cian marks muscle with phalloidin, magenta marks neuronal plasma membrane with HRP antibodies, and yellow mitochondria with the UAS-mitochondria-GFP transgene. Box plot depicts the ratio in between the mitochondrial signal and the HRP signal. Comparisons between genotypes were performed with One-Way ANOVA followed by Fishers's multiple comparison. Bar represents 50 µm

Fig.7. Hemideficiency of the *Drosophila* SLC25A4-sesB Alters Synapse Function.

Muscle VI-VII third instar neuromuscular junctions from w1118 control (gray traces) and *sesB* mutants (blue traces) were analyzed for evoked (EJP in A) and spontaneous neurotransmission (mEJP in B). C and D present amplitudes as dot plots with each dot corresponding to one animal. Lines depicts the mean of the sample. E) Neuromuscular junctions stimulated at low frequency (3 Hz, E) and high frequency (10 Hz, F-H) in the presence of 1µM bafilomycin A1 to assess recycling and reserve pools of synaptic vesicles. Graphs E-H show control animals as black symbols (w1118, E-G; w1118>C155, H), blue symbols show *sesB* mutants (F-G), and neuronal specific sesB RNAi (H, C155>sesB RNAi). Average±SEM. I-J) shows quantitation of graphs E-H as time (measured as stimulus number) to 50% depletion (Tau) compared to response at time/stimulus 0. I) correspond to synapses stimulated at 3Hz, recycling pool of vesicles while J) shows results for synapses stimulated at 10Hz, reserve pool of vesicles. Number of animal is shown in the bar bottom. Average ± SEM. K) Tau statistical

differences among genotypes at 3Hz (upper panel) and 10Hz (lower panel) represented as heat maps. Italic numbers depict genotypes in I) and J). All comparisons in I and J were performed with One-Way ANOVA followed by Fishers's multiple comparison.

Fig. 8. SLC25A1 and SLC25A4 are Necessary for Calcium Homeostasis.

A) Representative traces of mitochondrial Ca^{2+} uptake in permeabilized Hap1 cells challenged with 5 µM free Ca^{2+}. Mitochondrial Rhod2 fluorescence (F/F_0) was measured as function of time (s). B) Quantification of the maximal rates of mitochondrial calcium influx $\Delta F/F_0/s$ in control and mutant Hap1 cell lines. Comparisons between genotypes were performed with One-Way ANOVA followed by Fishers's multiple comparisons. C) qRT-PCR quantification of transcripts (x axis) in *Drosophila* heads of control animals carrying the Actin-Gal4 driver alone or in combination with the UAS-RNAi for SLC25A1-sea or SLC25A4-sesB transgenes (n=4, One Way ANOVA followed by Fisher's Least Significant Difference Comparison). D) mEJPs traces, E) amplitudes, and F) frequency at low and high extracellular calcium. Number of animals are listed at the base of columns in E apply to F, genotypes are listed on top of traces. E) P values for columns listed with italics at the base were determined by Between Subjects ANOVA followed by Bonferroni-Dunn Test: comparison a and b=0.0014, a to c=0.8421, e to f=0.0008, e to g=0.0026, f to g=0.6967. G) Pulsed paired facilitation traces at low and high calcium concentrations. H) Amplitude of the first EJP (P1). Number of animals are listed at the base of columns in H apply to I, genotypes are listed on top of traces. I) Ratios of the two pulses. P values were determined by Between Subjects ANOVA followed by Bonferroni-Dunn Test.

Fig. 9. The *Drosophila* SLC25A4 Orthologue, *sesB,* is Required in Glutamatergic Neurons for Sleep.

A) Individual hypnograms of two Canton S control and two *sesB* mutant flies illustrate sleep-wake activity patterns across the 12:12 hour light (zeitgeber times ZT1 to 12) and dark (zeitgeber times ZT12 to 24) periods. B) Heat map of sleep-wake activity (gray and teal, respectively) in Canton S control (n=229), ses^{org} (n=234), and $sesB^{9ed\text{-}1/+}$ (n=53) depict the activity for each animal averaged across one hour bins. Each column is one zeitgeber hour and each row an animal. C-G) Probability plots of sleep parameters per 24 hours (C, D and G) or 12 hours light/darkness periods (E and F) from animals depicted in B. TST is total sleeping time. H) The number of sleep bouts per 24 hours is increased by *sesB* RNAi targeted to glutamatergic neurons (CS=78, VGlut>CS=72, VGlut>RNAi=82 animals) but neither in I) glial cells (CS=78, repo>CS=53, repo>RNAi=59 animals), nor J) catecholaminergic neurons (CS=21, Ddc>CS=37, Ddc>RNAi=56 animals). C-J) p values were estimated with the Kolmogorov–Smirnov test. Similar analysis in *sea* RNAi animals is presented in Fig. 9-1.

Fig. 9-1. *Drosophila* SLC25A1 Orthologue *Sea* is Required in Catecholaminergic Neurons for Sleep.

A) Individual hypnograms of Canton S control, *sea* RNAi controls, and catecholaminergic-specific *sea* RNAi (Ddc>RNAi) flies (n=2 each) illustrates sleep-wake activity patterns across the 12:12 hour light (zeitgeber times ZT1 to 12) and dark (zeitgeber times ZT12 to 24) periods. B) Heat maps of sleep-wake activity (gray and teal, respectively) in *Ddc driver* control (Ddc>CS, n=56), *sea RNAi* control (n=40), and catecholaminergic-specific *sea* RNAi animals (Ddc>RNAi, n=40) depict activity for each animal averaged across one hour bins. Each column is one zeitgeber hour and each row is one animal. C-H) Probability plots of sleep parameters per 24 hours (C, D and G) or 12 hours light/dark periods (E, F and H) from animals depicted in B. TST is total sleeping time. G-H) The number of sleep bouts is decreased in catecholaminergic-specific *sea* RNAi animals. No effect of glutamatergic-specific *sea* RNAi (VGlut>CS=38, sea RNAi=40, VGlut>RNAi= 44 animals) C-J) p values were estimated with the Kolmogorov–Smirnov test

Table 1. Primers Used in these Studies.

References

Anders S, Pyl PT, Huber W (2015) HTSeq--a Python framework to work with high-throughput sequencing data. Bioinformatics 31:166-169.

Andrews S (2012) FASTQC In.

Anglin RE, Tarnopolsky MA, Mazurek MF, Rosebush PI (2012a) The psychiatric presentation of mitochondrial disorders in adults. J Neuropsychiatry Clin Neurosci 24:394-409.

Anglin RE, Garside SL, Tarnopolsky MA, Mazurek MF, Rosebush PI (2012b) The psychiatric manifestations of mitochondrial disorders: a case and review of the literature. J Clin Psychiatry 73:506-512.

Arion D, Corradi JP, Tang S, Datta D, Boothe F, He A, Cacace AM, Zaczek R, Albright CF, Tseng G, Lewis DA (2015) Distinctive transcriptome alterations of prefrontal pyramidal neurons in schizophrenia and schizoaffective disorder. Molecular psychiatry 20:1397-1405.

Bandiera S, Ruberg S, Girard M, Cagnard N, Hanein S, Chretien D, Munnich A, Lyonnet S, Henrion-Caude A (2011) Nuclear outsourcing of RNA interference components to human mitochondria. PloS one 6:e20746.

Bassett AS, Chow EW (2008) Schizophrenia and 22q11.2 deletion syndrome. Curr Psychiatry Rep 10:148-157.

Bassett AS, Chow EW, Weksberg R (2000) Chromosomal abnormalities and schizophrenia. American journal of medical genetics 97:45-51.

Bassett AS, Chow EW, AbdelMalik P, Gheorghiu M, Husted J, Weksberg R (2003) The schizophrenia phenotype in 22q11 deletion syndrome. The American journal of psychiatry 160:1580-1586.

Bena F et al. (2013) Molecular and clinical characterization of 25 individuals with exonic deletions of NRXN1 and comprehensive review of the literature. American journal of medical genetics Part B, Neuropsychiatric genetics : the official publication of the International Society of Psychiatric Genetics 162B:388-403.

Bers DM, Patton CW, Nuccitelli R (2010) A practical guide to the preparation of Ca(2+) buffers. Methods Cell Biol 99:1-26.

Bindea G, Mlecnik B, Hackl H, Charoentong P, Tosolini M, Kirilovsky A, Fridman WH, Pages F, Trajanoski Z, Galon J (2009) ClueGO: a Cytoscape plug-in to decipher functionally grouped gene ontology and pathway annotation networks. Bioinformatics 25:1091-1093.

Burkhardt C, Kelly JP, Lim YH, Filley CM, Parker WD, Jr. (1993) Neuroleptic medications inhibit complex I of the electron transport chain. Annals of neurology 33:512-517.

Butcher NJ, Kiehl TR, Hazrati LN, Chow EW, Rogaeva E, Lang AE, Bassett AS (2013) Association between early-onset Parkinson disease and 22q11.2 deletion syndrome: identification of a novel genetic form of Parkinson disease and its clinical implications. JAMA Neurol 70:1359-1366.

Butcher NJ, Marras C, Pondal M, Rusjan P, Boot E, Christopher L, Repetto GM, Fritsch R, Chow EWC, Masellis M, Strafella AP, Lang AE, Bassett AS (2017) Neuroimaging and clinical features in adults with a 22q11.2 deletion at risk of Parkinson's disease. Brain : a journal of neurology 140:1371-1383.

1353 Calvo SE, Clauser KR, Mootha VK (2016) MitoCarta2.0: an updated inventory of mammalian
1354 mitochondrial proteins. Nucleic acids research 44:D1251-1257.
1355 Campbell RA, Turner GC (2010) The mushroom body. Current biology : CB 20:R11-12.
1356 Chan SY, Zhang YY, Hemann C, Mahoney CE, Zweier JL, Loscalzo J (2009) MicroRNA-210 controls
1357 mitochondrial metabolism during hypoxia by repressing the iron-sulfur cluster assembly
1358 proteins ISCU1/2. Cell Metab 10:273-284.
1359 Chen CL, Hu Y, Udeshi ND, Lau TY, Wirtz-Peitz F, He L, Ting AY, Carr SA, Perrimon N (2015)
1360 Proteomic mapping in live Drosophila tissues using an engineered ascorbate peroxidase.
1361 Proceedings of the National Academy of Sciences of the United States of America
1362 112:12093-12098.
1363 Chen EY, Tan CM, Kou Y, Duan Q, Wang Z, Meirelles GV, Clark NR, Ma'ayan A (2013) Enrichr:
1364 interactive and collaborative HTML5 gene list enrichment analysis tool. BMC
1365 bioinformatics 14:128.
1366 Chouinard S, Poulin J, Stip E, Godbout R (2004) Sleep in untreated patients with schizophrenia:
1367 a meta-analysis. Schizophrenia bulletin 30:957-967.
1368 Crabtree GW, Park AJ, Gordon JA, Gogos JA (2016) Cytosolic Accumulation of L-Proline Disrupts
1369 GABA-Ergic Transmission through GAD Blockade. Cell reports 17:570-582.
1370 Crocker A, Guan XJ, Murphy CT, Murthy M (2016) Cell-Type-Specific Transcriptome Analysis in
1371 the Drosophila Mushroom Body Reveals Memory-Related Changes in Gene Expression.
1372 Cell reports 15:1580-1596.
1373 del Rio G, Koschutzki D, Coello G (2009) How to identify essential genes from molecular
1374 networks? BMC systems biology 3:102.
1375 Delgado R, Maureira C, Oliva C, Kidokoro Y, Labarca P (2000) Size of vesicle pools, rates of
1376 mobilization, and recycling at neuromuscular synapses of a Drosophila mutant, shibire.
1377 Neuron 28:941-953.
1378 Devaraju P, Zakharenko SS (2017) Mitochondria in complex psychiatric disorders: Lessons from
1379 mouse models of 22q11.2 deletion syndrome: Hemizygous deletion of several
1380 mitochondrial genes in the 22q11.2 genomic region can lead to symptoms associated
1381 with neuropsychiatric disease. Bioessays 39.
1382 Devaraju P, Yu J, Eddins D, Mellado-Lagarde MM, Earls LR, Westmoreland JJ, Quarato G, Green
1383 DR, Zakharenko SS (2017) Haploinsufficiency of the 22q11.2 microdeletion gene Mrpl40
1384 disrupts short-term synaptic plasticity and working memory through dysregulation of
1385 mitochondrial calcium. Molecular psychiatry 22:1313-1326.
1386 DiMauro S, Schon EA (2008) Mitochondrial disorders in the nervous system. Annual review of
1387 neuroscience 31:91-123.
1388 Elmorsy E, Smith PA (2015) Bioenergetic disruption of human micro-vascular endothelial cells
1389 by antipsychotics. Biochemical and biophysical research communications 460:857-862.
1390 Enwright Iii JF, Huo Z, Arion D, Corradi JP, Tseng G, Lewis DA (2017) Transcriptome alterations of
1391 prefrontal cortical parvalbumin neurons in schizophrenia. Molecular psychiatry.
1392 Floyd BJ et al. (2016) Mitochondrial Protein Interaction Mapping Identifies Regulators of
1393 Respiratory Chain Function. Molecular cell 63:621-632.
1394 Frank CA, Wang X, Collins CA, Rodal AA, Yuan Q, Verstreken P, Dickman DK (2013) New
1395 approaches for studying synaptic development, function, and plasticity using Drosophila

1396 as a model system. The Journal of neuroscience : the official journal of the Society for
1397 Neuroscience 33:17560-17568.
1398 Freeman A, Pranski E, Miller RD, Radmard S, Bernhard D, Jinnah HA, Betarbet R, Rye DB, Sanyal
1399 S (2012) Sleep fragmentation and motor restlessness in a Drosophila model of Restless
1400 Legs Syndrome. Current biology : CB 22:1142-1148.
1401 Gandal MJ, Haney JR, Parikshak NN, Leppa V, Ramaswami G, Hartl C, Schork AJ, Appadurai V,
1402 Buil A, Werge TM, Liu C, White KP, CommonMind C, Psych EC, i P-BWG, Horvath S,
1403 Geschwind DH (2018) Shared molecular neuropathology across major psychiatric
1404 disorders parallels polygenic overlap. Science 359:693-697.
1405 Girirajan S, Campbell CD, Eichler EE (2011) Human copy number variation and complex genetic
1406 disease. Annual review of genetics 45:203-226.
1407 Guna A, Butcher NJ, Bassett AS (2015) Comparative mapping of the 22q11.2 deletion region and
1408 the potential of simple model organisms. J Neurodev Disord 7:18.
1409 Guo X, Macleod GT, Wellington A, Hu F, Panchumarthi S, Schoenfield M, Marin L, Charlton MP,
1410 Atwood HL, Zinsmaier KE (2005) The GTPase dMiro is required for axonal transport of
1411 mitochondria to Drosophila synapses. Neuron 47:379-393.
1412 Havugimana PC et al. (2012) A census of human soluble protein complexes. Cell 150:1068-1081.
1413 Hein MY, Hubner NC, Poser I, Cox J, Nagaraj N, Toyoda Y, Gak IA, Weisswange I, Mansfeld J,
1414 Buchholz F, Hyman AA, Mann M (2015) A human interactome in three quantitative
1415 dimensions organized by stoichiometries and abundances. Cell 163:712-723.
1416 Hendricks JC, Finn SM, Panckeri KA, Chavkin J, Williams JA, Sehgal A, Pack AI (2000) Rest in
1417 Drosophila is a sleep-like state. Neuron 25:129-138.
1418 Hodgkinson KA, Murphy J, O'Neill S, Brzustowicz L, Bassett AS (2001) Genetic counselling for
1419 schizophrenia in the era of molecular genetics. Can J Psychiatry 46:123-130.
1420 Hoeffding LK, Trabjerg BB, Olsen L, Mazin W, Sparso T, Vangkilde A, Mortensen PB, Pedersen
1421 CB, Werge T (2017) Risk of Psychiatric Disorders Among Individuals With the 22q11.2
1422 Deletion or Duplication: A Danish Nationwide, Register-Based Study. JAMA Psychiatry
1423 74:282-290.
1424 Huttlin EL et al. (2017) Architecture of the human interactome defines protein communities and
1425 disease networks. Nature 545:505-509.
1426 Huttlin EL et al. (2015) The BioPlex Network: A Systematic Exploration of the Human
1427 Interactome. Cell 162:425-440.
1428 International Schizophrenia C (2008) Rare chromosomal deletions and duplications increase risk
1429 of schizophrenia. Nature 455:237-241.
1430 Ishizuka K, Paek M, Kamiya A, Sawa A (2006) A review of Disrupted-In-Schizophrenia-1 (DISC1):
1431 neurodevelopment, cognition, and mental conditions. Biological psychiatry 59:1189-
1432 1197.
1433 Iyer J, Singh MD, Jensen M, Patel P, Pizzo L, Huber E, Koerselman H, Weiner AT, Lepanto P,
1434 Vadodaria K, Kubina A, Wang Q, Talbert A, Yennawar S, Badano J, Manak JR, Rolls MM,
1435 Krishnan A, Girirajan S (2018) Pervasive genetic interactions modulate
1436 neurodevelopmental defects of the autism-associated 16p11.2 deletion in Drosophila
1437 melanogaster. Nature communications 9:2548.
1438 Jalbrzikowski M, Lazaro MT, Gao F, Huang A, Chow C, Geschwind DH, Coppola G, Bearden CE
1439 (2015) Transcriptome Profiling of Peripheral Blood in 22q11.2 Deletion Syndrome

1440 Reveals Functional Pathways Related to Psychosis and Autism Spectrum Disorder. PloS
1441 one 10:e0132542.
1442 Jonas RK, Montojo CA, Bearden CE (2014) The 22q11.2 deletion syndrome as a window into
1443 complex neuropsychiatric disorders over the lifespan. Biological psychiatry 75:351-360.
1444 Kamath J, Virdi S, Winokur A (2015) Sleep Disturbances in Schizophrenia. Psychiatr Clin North
1445 Am 38:777-792.
1446 Karayiorgou M, Simon TJ, Gogos JA (2010) 22q11.2 microdeletions: linking DNA structural
1447 variation to brain dysfunction and schizophrenia. Nat Rev Neurosci 11:402-416.
1448 Kim SM, Kumar V, Lin YQ, Karunanithi S, Ramaswami M (2009) Fos and Jun potentiate individual
1449 release sites and mobilize the reserve synaptic vesicle pool at the Drosophila larval
1450 motor synapse. Proceedings of the National Academy of Sciences of the United States of
1451 America 106:4000-4005.
1452 Kirov G (2015) CNVs in neuropsychiatric disorders. Human molecular genetics.
1453 Klingenberg M (2008) The ADP and ATP transport in mitochondria and its carrier. Biochimica et
1454 biophysica acta 1778:1978-2021.
1455 Krakowiak P, Goodlin-Jones B, Hertz-Picciotto I, Croen LA, Hansen RL (2008) Sleep problems in
1456 children with autism spectrum disorders, developmental delays, and typical
1457 development: a population-based study. J Sleep Res 17:197-206.
1458 Langmead B, Salzberg SL (2012) Fast gapped-read alignment with Bowtie 2. Nature methods
1459 9:357-359.
1460 Levy M, Faas GC, Saggau P, Craigen WJ, Sweatt JD (2003) Mitochondrial regulation of synaptic
1461 plasticity in the hippocampus. The Journal of biological chemistry 278:17727-17734.
1462 Lin MT, Beal MF (2006) Mitochondrial dysfunction and oxidative stress in neurodegenerative
1463 diseases. Nature 443:787-795.
1464 Love MI, Huber W, Anders S (2014) Moderated estimation of fold change and dispersion for
1465 RNA-seq data with DESeq2. Genome biology 15:550.
1466 Lu YW, Acoba MG, Selvaraju K, Huang TC, Nirujogi RS, Sathe G, Pandey A, Claypool SM (2017)
1467 Human adenine nucleotide translocases physically and functionally interact with
1468 respirasomes. Molecular biology of the cell 28:1489-1506.
1469 Malhotra D, Sebat J (2012) CNVs: harbingers of a rare variant revolution in psychiatric genetics.
1470 Cell 148:1223-1241.
1471 Marshall CR et al. (2017) Contribution of copy number variants to schizophrenia from a
1472 genome-wide study of 41,321 subjects. Nature genetics 49:27-35.
1473 Maxwell JT, Tsai CH, Mohiuddin TA, Kwong JQ (2018) Analyses of Mitochondrial Calcium Influx
1474 in Isolated Mitochondria and Cultured Cells. J Vis Exp.
1475 Maynard TM, Meechan DW, Dudevoir ML, Gopalakrishna D, Peters AZ, Heindel CC, Sugimoto TJ,
1476 Wu Y, Lieberman JA, Lamantia AS (2008) Mitochondrial localization and function of a
1477 subset of 22q11 deletion syndrome candidate genes. Molecular and cellular
1478 neurosciences 39:439-451.
1479 McDonald-McGinn DM, Sullivan KE, Marino B, Philip N, Swillen A, Vorstman JA, Zackai EH,
1480 Emanuel BS, Vermeesch JR, Morrow BE, Scambler PJ, Bassett AS (2015) 22q11.2 deletion
1481 syndrome. Nat Rev Dis Primers 1:15071.

1482 Middleton FA, Mirnics K, Pierri JN, Lewis DA, Levitt P (2002) Gene expression profiling reveals
1483 alterations of specific metabolic pathways in schizophrenia. The Journal of neuroscience
1484 : the official journal of the Society for Neuroscience 22:2718-2729.
1485 Minones-Moyano E, Porta S, Escaramis G, Rabionet R, Iraola S, Kagerbauer B, Espinosa-Parrilla
1486 Y, Ferrer I, Estivill X, Marti E (2011) MicroRNA profiling of Parkinson's disease brains
1487 identifies early downregulation of miR-34b/c which modulate mitochondrial function.
1488 Human molecular genetics 20:3067-3078.
1489 Modica-Napolitano JS, Lagace CJ, Brennan WA, Aprille JR (2003) Differential effects of typical
1490 and atypical neuroleptics on mitochondrial function in vitro. Arch Pharm Res 26:951-
1491 959.
1492 Mok KY et al. (2016) Deletions at 22q11.2 in idiopathic Parkinson's disease: a combined analysis
1493 of genome-wide association data. Lancet neurology 15:585-596.
1494 Monti JM, Monti D (2004) Sleep in schizophrenia patients and the effects of antipsychotic
1495 drugs. Sleep Med Rev 8:133-148.
1496 Morciano P, Carrisi C, Capobianco L, Mannini L, Burgio G, Cestra G, De Benedetto GE, Corona
1497 DF, Musio A, Cenci G (2009) A conserved role for the mitochondrial citrate transporter
1498 Sea/SLC25A1 in the maintenance of chromosome integrity. Human molecular genetics
1499 18:4180-4188.
1500 Mullin AP, Sadanandappa MK, Ma W, Dickman DK, VijayRaghavan K, Ramaswami M, Sanyal S,
1501 Faundez V (2015) Gene dosage in the dysbindin schizophrenia susceptibility network
1502 differentially affect synaptic function and plasticity. The Journal of neuroscience : the
1503 official journal of the Society for Neuroscience 35:325-338.
1504 Norkett R, Modi S, Kittler JT (2017) Mitochondrial roles of the psychiatric disease risk factor
1505 DISC1. Schizophrenia research 187:47-54.
1506 Pagliarini DJ, Calvo SE, Chang B, Sheth SA, Vafai SB, Ong SE, Walford GA, Sugiana C, Boneh A,
1507 Chen WK, Hill DE, Vidal M, Evans JG, Thorburn DR, Carr SA, Mootha VK (2008) A
1508 mitochondrial protein compendium elucidates complex I disease biology. Cell 134:112-
1509 123.
1510 Palmieri F, Monne M (2016) Discoveries, metabolic roles and diseases of mitochondrial carriers:
1511 A review. Biochimica et biophysica acta 1863:2362-2378.
1512 Paterlini M, Zakharenko SS, Lai WS, Qin J, Zhang H, Mukai J, Westphal KG, Olivier B, Sulzer D,
1513 Pavlidis P, Siegelbaum SA, Karayiorgou M, Gogos JA (2005) Transcriptional and
1514 behavioral interaction between 22q11.2 orthologs modulates schizophrenia-related
1515 phenotypes in mice. Nature neuroscience 8:1586-1594.
1516 Petrovsky N, Ettinger U, Hill A, Frenzel L, Meyhofer I, Wagner M, Backhaus J, Kumari V (2014)
1517 Sleep deprivation disrupts prepulse inhibition and induces psychosis-like symptoms in
1518 healthy humans. The Journal of neuroscience : the official journal of the Society for
1519 Neuroscience 34:9134-9140.
1520 Ping L, Duong DM, Yin L, Gearing M, Lah JJ, Levey AI, Seyfried NT (2018) Global quantitative
1521 analysis of the human brain proteome in Alzheimer's and Parkinson's Disease. Sci Data
1522 5:180036.
1523 Prince JA, Yassin MS, Oreland L (1997) Neuroleptic-induced mitochondrial enzyme alterations in
1524 the rat brain. The Journal of pharmacology and experimental therapeutics 280:261-267.

1525 Regehr WG (2012) Short-term presynaptic plasticity. Cold Spring Harbor perspectives in biology
1526 4:a005702.
1527 Rikhy R, Ramaswami M, Krishnan KS (2003) A temperature-sensitive allele of Drosophila sesB
1528 reveals acute functions for the mitochondrial adenine nucleotide translocase in synaptic
1529 transmission and dynamin regulation. Genetics 165:1243-1253.
1530 Rosenfeld M, Brenner-Lavie H, Ari SG, Kavushansky A, Ben-Shachar D (2011) Perturbation in
1531 mitochondrial network dynamics and in complex I dependent cellular respiration in
1532 schizophrenia. Biological psychiatry 69:980-988.
1533 Rutkowski TP, Schroeder JP, Gafford GM, Warren ST, Weinshenker D, Caspary T, Mulle JG
1534 (2017) Unraveling the genetic architecture of copy number variants associated with
1535 schizophrenia and other neuropsychiatric disorders. Journal of neuroscience research
1536 95:1144-1160.
1537 Santoro MR, Bray SM, Warren ST (2012) Molecular mechanisms of fragile X syndrome: a
1538 twenty-year perspective. Annual review of pathology 7:219-245.
1539 Schneider M et al. (2014) Psychiatric Disorders From Childhood to Adulthood in 22q11.2
1540 Deletion Syndrome: Results From the International Consortium on Brain and Behavior in
1541 22q11.2 Deletion Syndrome. The American journal of psychiatry.
1542 Sheng ZH, Cai Q (2012) Mitochondrial transport in neurons: impact on synaptic homeostasis
1543 and neurodegeneration. Nat Rev Neurosci 13:77-93.
1544 Stark KL, Xu B, Bagchi A, Lai WS, Liu H, Hsu R, Wan X, Pavlidis P, Mills AA, Karayiorgou M, Gogos
1545 JA (2008) Altered brain microRNA biogenesis contributes to phenotypic deficits in a
1546 22q11-deletion mouse model. Nature genetics 40:751-760.
1547 Sullivan PF, Daly MJ, O'Donovan M (2012) Genetic architectures of psychiatric disorders: the
1548 emerging picture and its implications. Nature reviews Genetics.
1549 Sztainberg Y, Zoghbi HY (2016) Lessons learned from studying syndromic autism spectrum
1550 disorders. Nature neuroscience 19:1408-1417.
1551 Taylor EB (2017) Functional Properties of the Mitochondrial Carrier System. Trends in cell
1552 biology 27:633-644.
1553 Verstreken P, Ly CV, Venken KJ, Koh TW, Zhou Y, Bellen HJ (2005) Synaptic mitochondria are
1554 critical for mobilization of reserve pool vesicles at Drosophila neuromuscular junctions.
1555 Neuron 47:365-378.
1556 Vos M, Lauwers E, Verstreken P (2010) Synaptic mitochondria in synaptic transmission and
1557 organization of vesicle pools in health and disease. Front Synaptic Neurosci 2:139.
1558 Wan C et al. (2015) Panorama of ancient metazoan macromolecular complexes. Nature
1559 525:339-344.
1560 Weeber EJ, Levy M, Sampson MJ, Anflous K, Armstrong DL, Brown SE, Sweatt JD, Craigen WJ
1561 (2002) The role of mitochondrial porins and the permeability transition pore in learning
1562 and synaptic plasticity. The Journal of biological chemistry 277:18891-18897.
1563 Wen Z et al. (2014) Synaptic dysregulation in a human iPS cell model of mental disorders.
1564 Nature 515:414-418.
1565 Wesseling H, Xu B, Want EJ, Holmes E, Guest PC, Karayiorgou M, Gogos JA, Bahn S (2017)
1566 System-based proteomic and metabonomic analysis of the Df(16)A(+/-) mouse identifies
1567 potential miR-185 targets and molecular pathway alterations. Molecular psychiatry
1568 22:384-395.

1569 Wu L, Candille SI, Choi Y, Xie D, Jiang L, Li-Pook-Than J, Tang H, Snyder M (2013) Variation and
1570 genetic control of protein abundance in humans. Nature 499:79-82.
1571 Zaleski C, Bassett AS, Tam K, Shugar AL, Chow EW, McPherson E (2009) The co-occurrence of
1572 early onset Parkinson disease and 22q11.2 deletion syndrome. American journal of
1573 medical genetics Part A 149A:525-528.
1574 Zhang X, Zuo X, Yang B, Li Z, Xue Y, Zhou Y, Huang J, Zhao X, Zhou J, Yan Y, Zhang H, Guo P, Sun
1575 H, Guo L, Zhang Y, Fu XD (2014) MicroRNA directly enhances mitochondrial translation
1576 during muscle differentiation. Cell 158:607-619.
1577 Zhang YQ, Roote J, Brogna S, Davis AW, Barbash DA, Nash D, Ashburner M (1999) stress
1578 sensitive B encodes an adenine nucleotide translocase in Drosophila melanogaster.
1579 Genetics 153:891-903.
1580 Zlatic SA, Vrailas-Mortimer A, Gokhale A, Carey LJ, Scott E, Burch R, McCall MM, Rudin-Rush S,
1581 Davis JB, Hartwig C, Werner E, Li L, Petris M, Faundez V (2018) Rare Disease Mechanisms
1582 Identified by Genealogical Proteomics of Copper Homeostasis Mutant Pedigrees. Cell
1583 Syst 6:368-380 e366.
1584

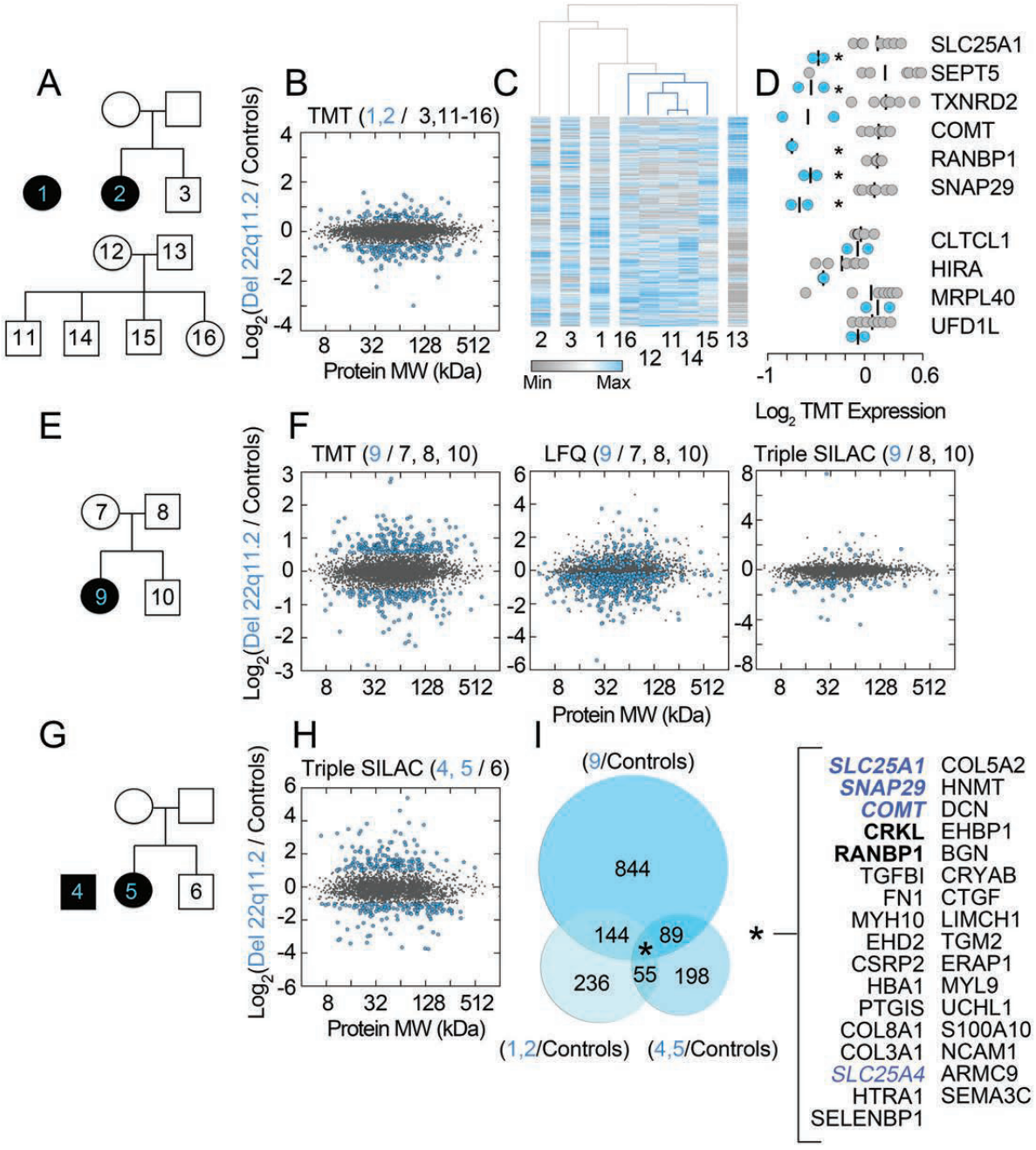

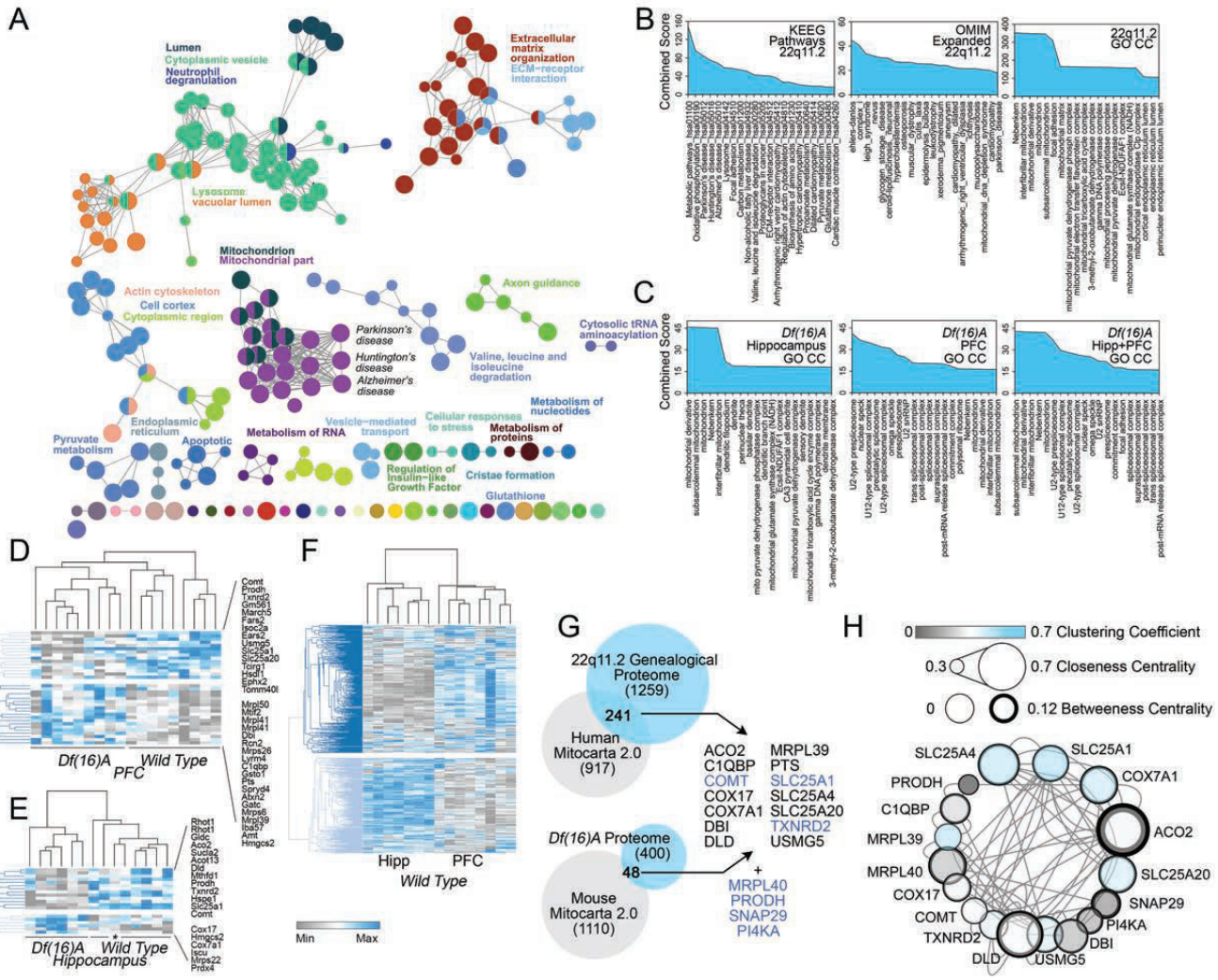

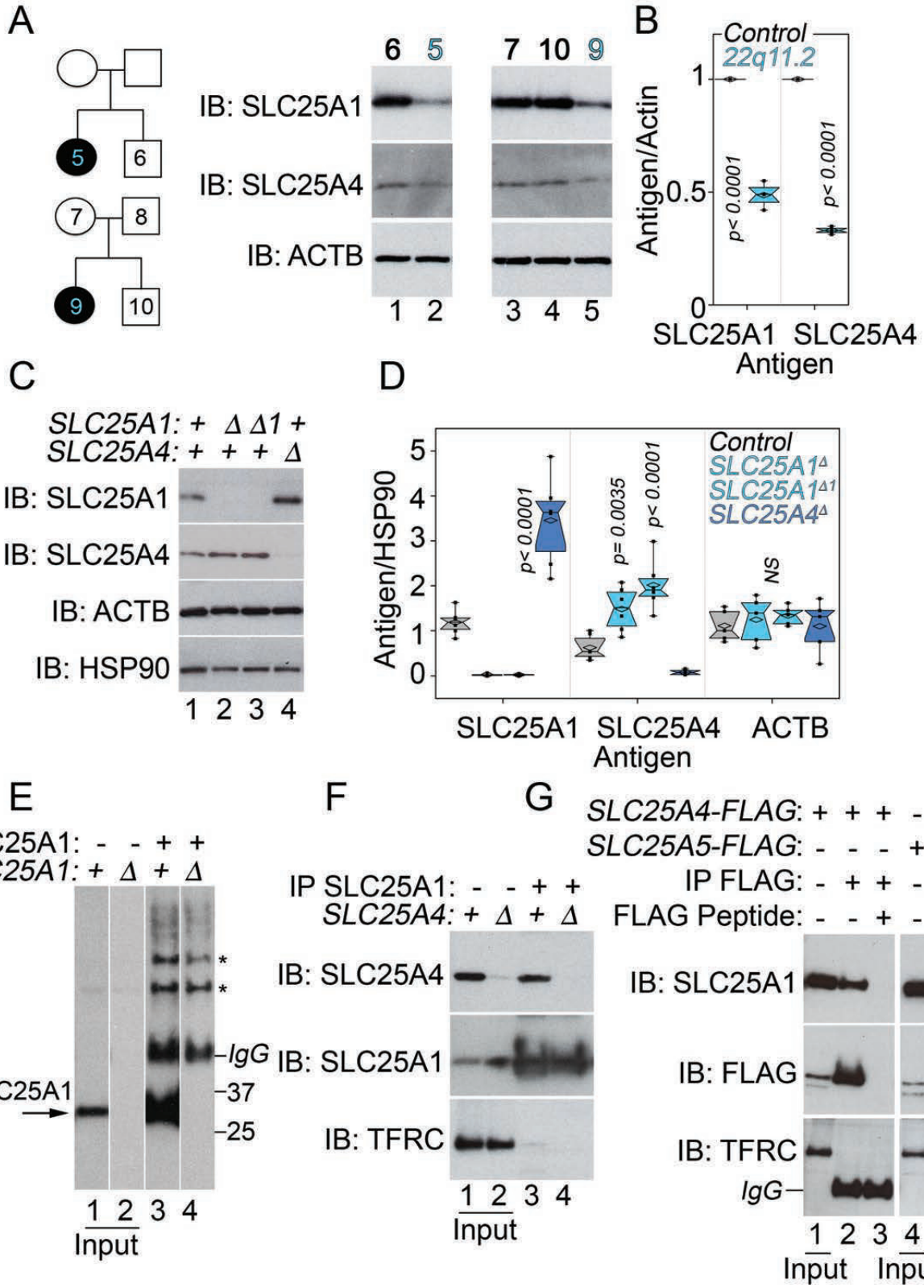

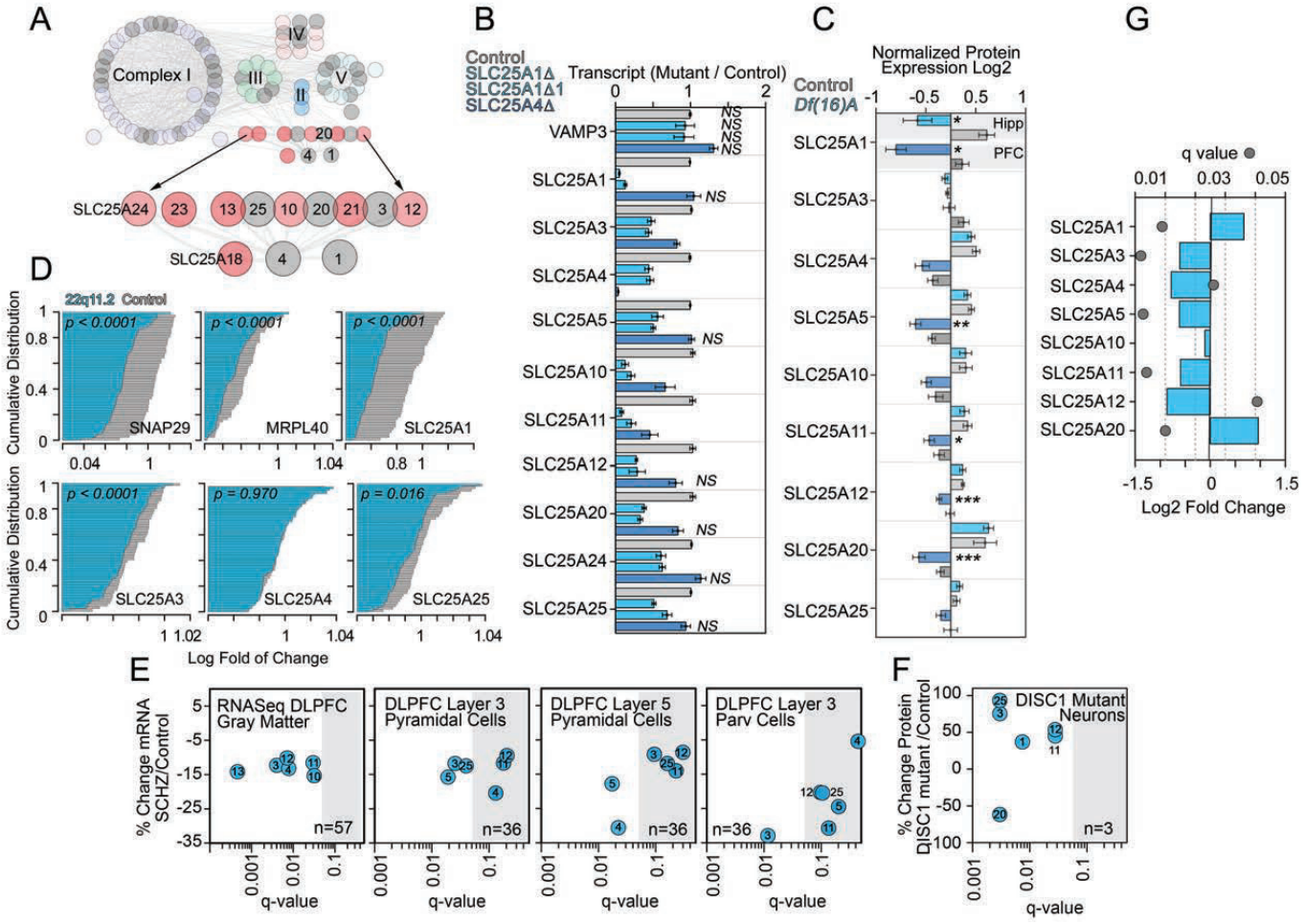

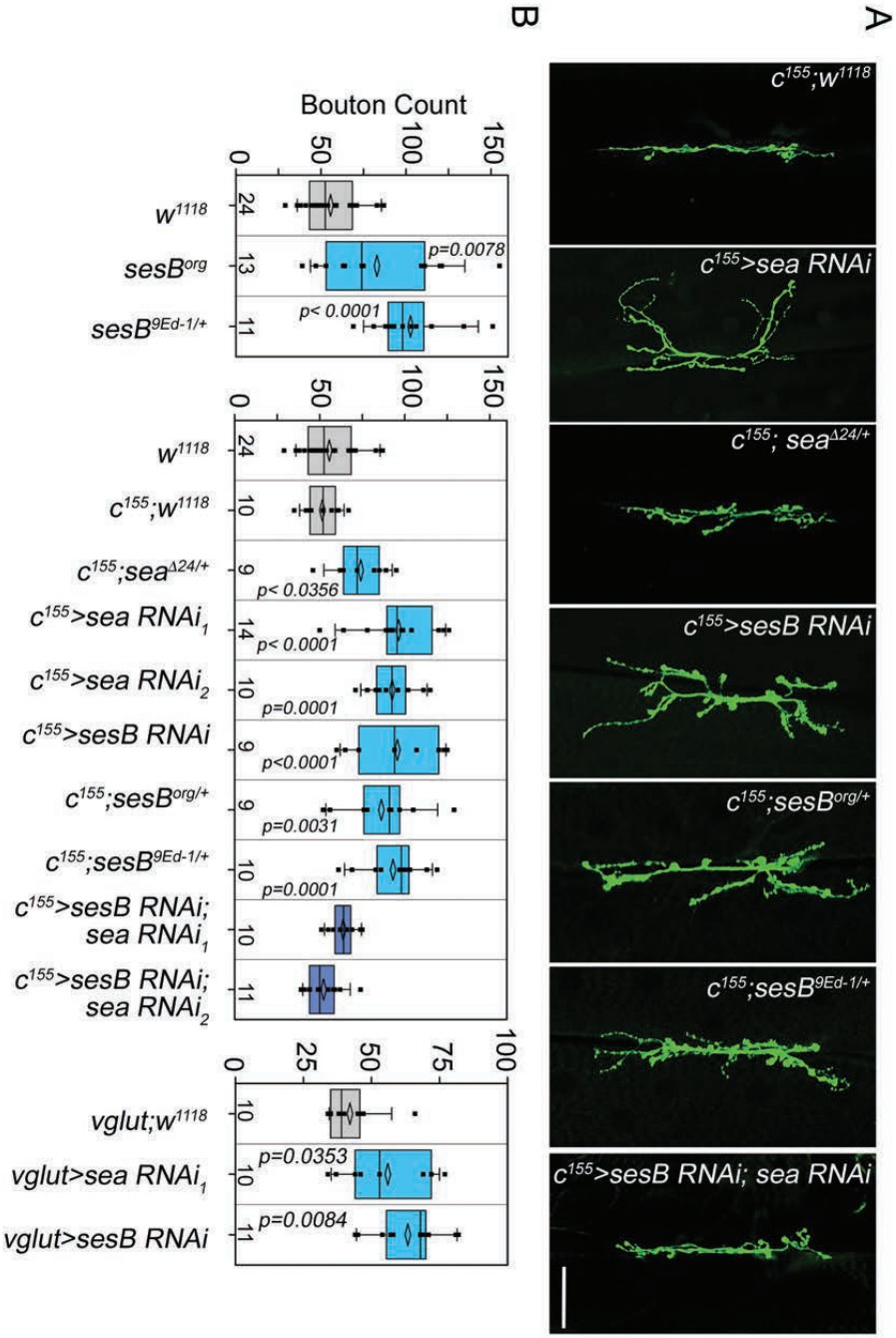
B
A
Bouton Count
0
50
100
150
w1118
sesBorg
sesB9Ed-1/+
24
13
11
p=0.0078
p< 0.0001
w1118
c155;w1118
c155;seaΔ24/+
c155>sea RNAi1
c155>sea RNAi2
c155>sesB RNAi
c155;sesBorg/+
c155;sesB9Ed-1/+
c155>sesB RNAi; sea RNAi1
c155>sesB RNAi; sea RNAi2
24
10
9
14
10
9
9
10
10
11
p< 0.0356
p< 0.0001
p=0.0001
p<0.0001
p=0.0031
p=0.0001
0
25
50
75
100
vglut;w1118
vglut>sea RNAi1
vglut>sesB RNAi
10
10
11
p=0.0353
p=0.0084
c155;w1118
c155>sea RNAi
c155; seaΔ24/+
c155>sesB RNAi
c155;sesBorg/+
c155;sesB9Ed-1/+
c155>sesB RNAi; sea RNAi

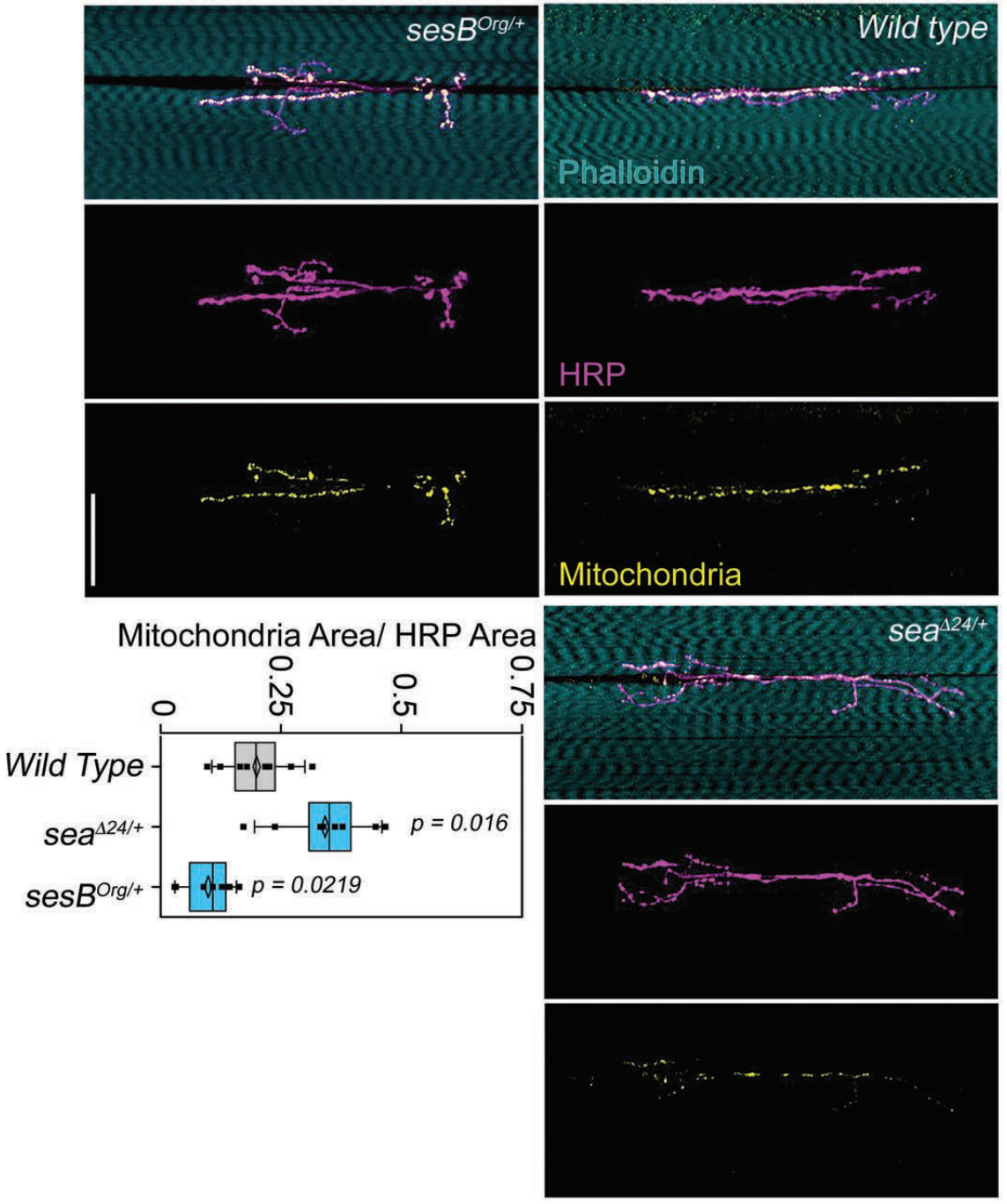
sesB^Org/+
Wild type
Phalloidin
HRP
Mitochondria
Mitochondria Area/ HRP Area
0
0.25
0.5
0.75
Wild Type
sea^Δ24/+
p = 0.016
sesB^Org/+
p = 0.0219
sea^Δ24/+

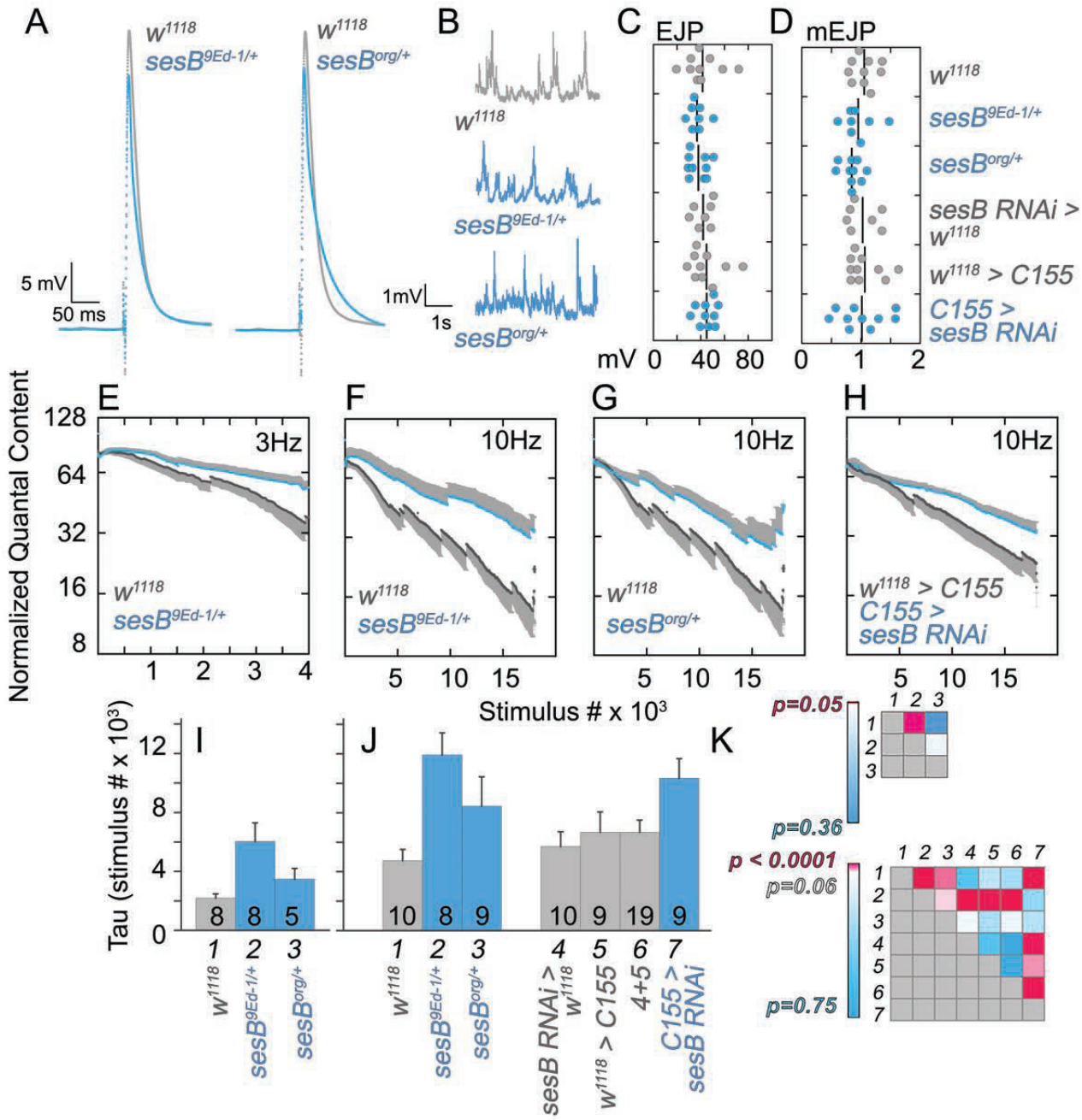

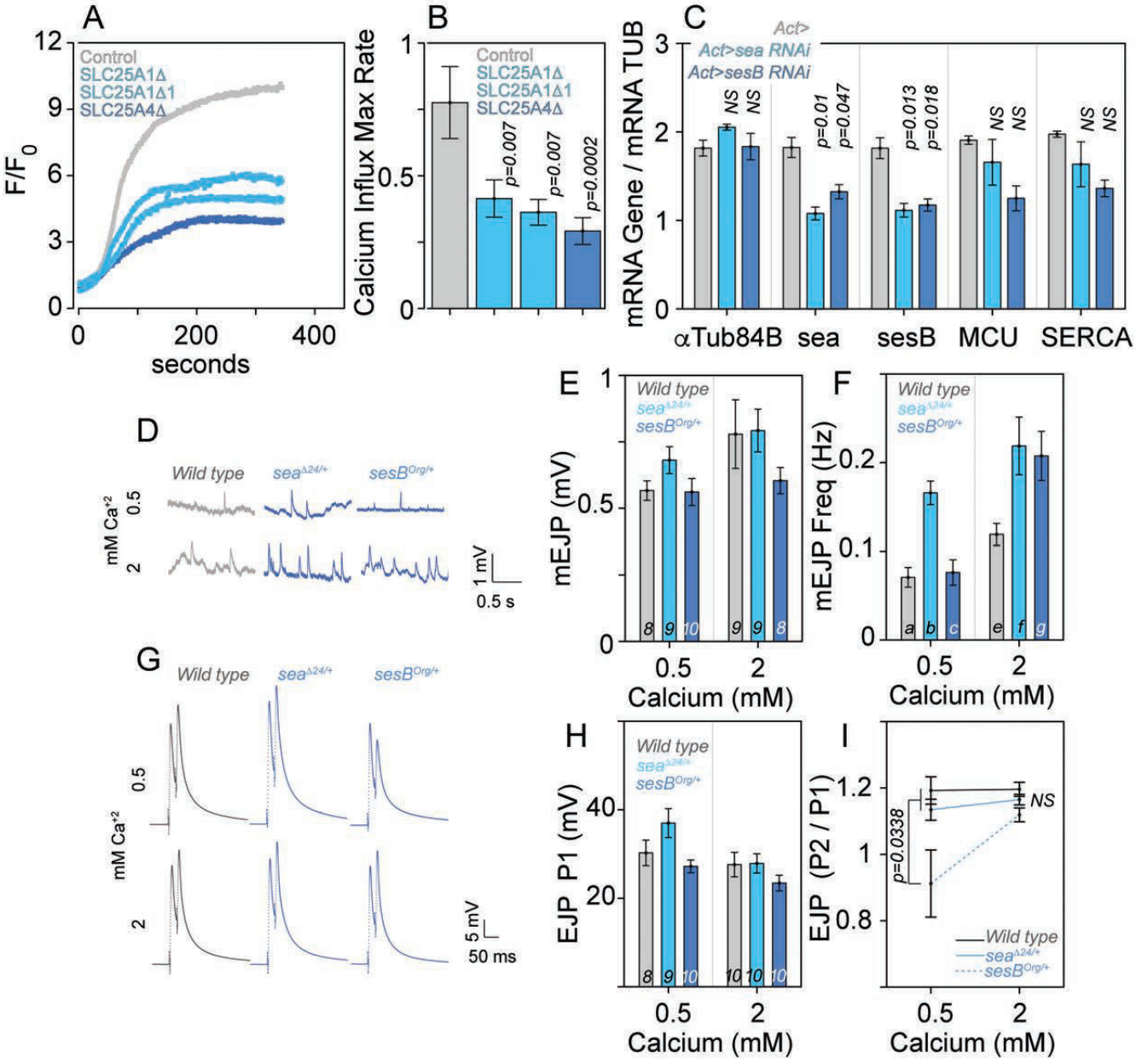

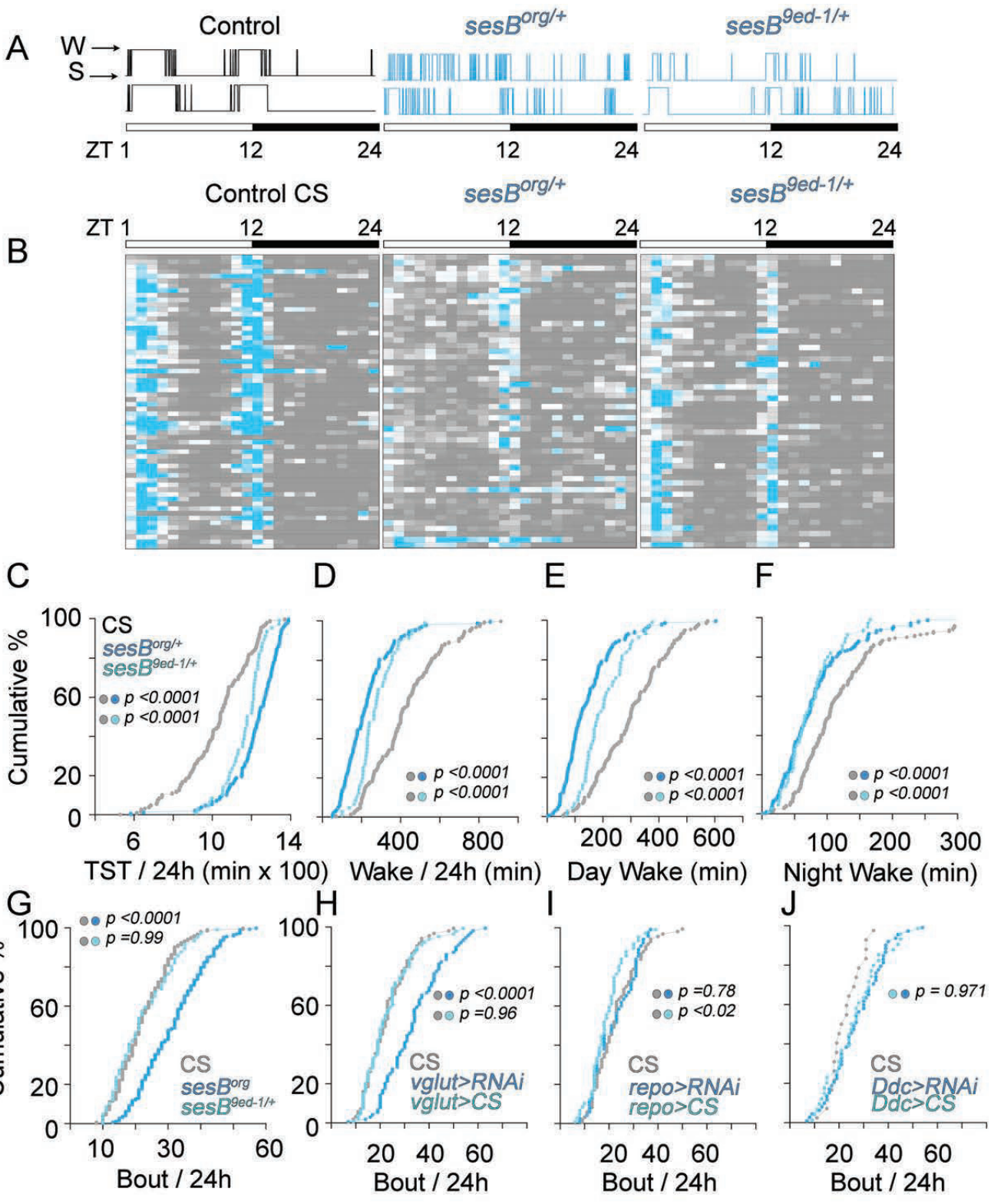

Transcript	*Species*	*Forward*	*Reverse*
SLC25A1	Hs	GTGTGGAAGACGGACTAAGC	ACTGGAATCGTGAGACAAAGG
SLC25A3	Hs	AGGATGGTGTTCGTGGTTTG	TGTGCGCCAGAGATAAGTATTC
SLC25A4	Hs	AGGGTTTCAACGTCTCTGTC	GTCACACTCTGGGCAATCAT
SLC25A5	Hs	CTGATGGGATTAAGGGCCTG	ACGATGTGAGTGTTCTTGGG
SLC25A10	Hs	ACTTGGTCAACGTCAGGATG	TTGCACCCGAGAACAGTC
SLC25A11	Hs	CCTAAGTCCGTCAAGTTCCTG	AGCTGGTTTTGTACTCTCGAG
SLC25A12	Hs	ACGCTATGGACAAGTCACAC	AGTTCTGCCAGGTTGTAAGG
SLC25A20	Hs	ATCAGCCCGCTCAAGAAC	GTCAAAGGTCCCAGAGTACATG
SLC25A24	Hs	TCTCGAACAAGCACTGCC	TGTACCATTTCCCCTCCAAAG
SLC25A25	Hs	GGCTGGTGTTTAAGAGTTTGG	TGGTCATCGTGCCGTTTT
VAMP3	Hs	TTGAGGTAGACTCTGACCGTCTC	GCTGGAGTCCACAGCTGATAAT
VIM	Hs	CGTGAATACCAAGACCTGCTC	GGAAAAGTTTGGAAGAGGCAG
αTub84B	Dm	TGTCGCGTGTGAAACACTTC	AGCAGGCGTTTCCAATCTG
Sea	Dm	CCTAAGTCAGCGGCGAGA	CCACGATGGCCTCACATAC
SesB	Dm	TTGTCTACCCCTTGGACTTTG	CTGACCACCCTTGCCAGT
MCU	Dm	TCCTGCACCATCGAAAGC	CCAATGTGCGATTGTTGATT
SERCA	Dm	CGAAATGTTGAACGCAATGA	AAGGAGAGTGCCATTGATCC